



FYS-3931

MASTER'S THESIS IN SPACE PHYSICS

Multifractals and Their Application to Geospace
Data

Lene Østvand

June, 2008

FACULTY OF SCIENCE
Department of Physics and Technology
University of Tromsø

FYS-3931

MASTER'S THESIS IN SPACE PHYSICS

Multifractals and Their Applications to Geospace
Data

Lene Østvand

June, 2008

Acknowledgments

First and foremost I would like to thank my advisor, professor Kristoffer Rypdal, for giving me an interesting project, providing numerous papers for me to read, giving a lot of feedback on my work and correcting everything from spelling mistakes to more critical errors. It has truly been inspiring to have Kristoffer as an advisor. He has really motivated me to “keep up the good work”, and I am very thankful for that.

I also would like to thank Tatjana Živković for tips concerning my analysis of the AE index, and for including my work in her contributed paper for Publ. Astron. Obs. Belgrade No. 87 (2008), 1 - 4.

My only classmate Joachim Knutsen must be thanked for all the interesting discussions we have had in our office. After starting on the master programme in space physics in 2003, we are the only two from our class that finish these studies. With 100 % of the students being from Drammen it is amazing that it has been going so well. Joachim must be especially thanked for the discussions concerning magnetospheric dynamics, but also for all the funny and a bit too long-lasting coffee breaks. With only two students in our class, I consider myself lucky that Joachim was the other one.

Finally, my boyfriend Jørn should be thanked for his support and belief in me, and for reading through my thesis. I am grateful that he has provided me food when I have been working late at the office, although he should be expected to cook, clean and not eat macaroons when (mistakenly) believing that I will provide for him when I am a rich, mad scientist.



Abstract

In this thesis I first introduce multifractal theory and mathematical concepts for multifractal analysis. Different methods for different uses are described, with focus on a differentiating between coarse and fine theory approaches. Methods for analysing time series are also described, more specifically a direct method based on the coarse theory analysis, the wavelet transform modulus maxima (WTMM) method and the multifractal detrended fluctuation analysis (MFDFA).

The next part of this thesis contains a selection of examples of applications of multifractals in science. Multifractal analysis have become very useful to describe properties of many phenomena in a wide range of fields, for instance space physics, medicine and finance, in addition to geology where fractal theory was first introduced.

Finally, I have analysed the three components of the interplanetary magnetic field strength at the Earth's bow shock nose, the AE index and the D_{st} index for solar cycle 23, lasting from 1996 to 2006 with a peak in 1999. Multifractality was found for the IMF data and the AE index, which may indicate that both the AE index and the interplanetary magnetic field have a intermittent and turbulent character. Multifractality for the D_{st} index was not shown as clearly, which indicates that this index is only weakly intermittent or not intermittent at all.

Contents

Acknowledgments	i
Abstract	iii
1 Introduction to the Mathematical Theory of Multifractals	1
2 Multifractals	5
2.1 Coarse Multifractal Theory	6
2.2 Fine Multifractal Theory	13
2.3 Multifractal Time Series	16
2.3.1 Wavelet Transform Modulus Maxima	16
2.3.2 Multifractal Detrended Fluctuation Analysis	18
3 A Random Walk Through Applications of Multifractals in Science	19
3.1 Geology	19
3.2 Space Physics	21
3.3 Biology	22
3.4 Chemistry	23
3.5 Medicine	25
3.6 Finance	25
4 Data Analysis	27
4.1 Sandpile	29
4.2 The Interplanetary Magnetic Field	32
4.3 The Auroral Electrojet Index	35
4.4 The Disturbance Storm Time Index	38
4.5 Results	39

4.6 Discussion	52
5 Conclusions	55
Appendices	57
Bibliography	97

Chapter 1

Introduction to the Mathematical Theory of Multifractals

Scale invariance is a well known term in geology [1]. Many geological phenomena are scale invariant, which means that they exist in many sizes, but still look the same, so it is impossible to tell of what size they are without any other objects with a characteristic dimension. Mandelbrot introduced the concept of fractals in this context in 1967. One example is a rocky coastline. Rocks look the same whether they are small sand grains or large boulders, so they are scale invariant within the range of sizes a rock may have. Without trees or houses, which have a characteristic dimension, one cannot tell the length of the rocky coastline. One can measure the length with a measuring rod with a specific length, but the length of the coastline will increase as the the length of the measuring rod decreases according to a power-law. The power determines the fractal dimension. The Koch curve (Figure 1.1) may be used as a model for a coastline. This has the typical features of a fractal. At high orders the structure seems quite complicated, and is hard to describe with classical geometry. At the first order, also called the generator of the fractal, the structure is actually very simple. The generator is used again on each line segment to construct the second order of the Koch curve, etc. Once you know the generator, it is easy to find the fractal dimension. At zero order the Koch curve is a flat line, and at first order this line is broken into four line segments with length $\frac{1}{3}$. At second order this operation is performed on each line segment, and we get 16 lines of length $\frac{1}{9}$. The similarity dimension is the dimension $\frac{-\log m}{\log r}$, where m is the number of copies the fractal set is made up of scaled by a factor r . The Koch curve has a similarity dimension $\frac{-\log 4}{\log \frac{1}{3}} = \frac{\log 4}{\log 3} \approx 1.2619$, which makes it larger than 1-dimensional (having infinite length) and smaller than 2-dimensional (having zero area). The length of the Koch curve is $\left(\frac{4}{3}\right)^k$, so after infinitely many iterations, the length goes towards in-

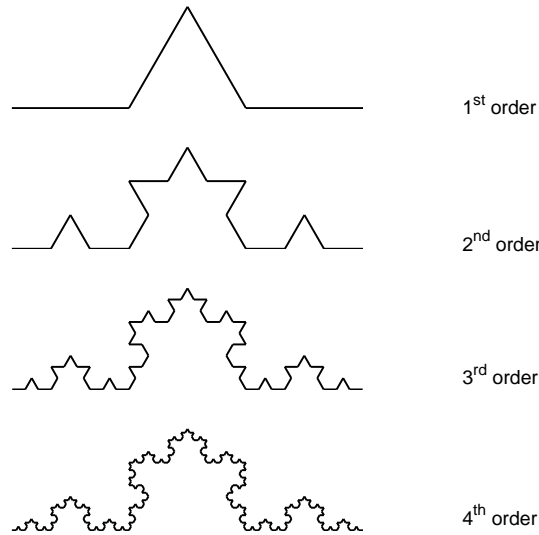


Figure 1.1: Koch curve carried to 4th order.

finitly.

The similarity dimension is meaningful only for strictly self-similar sets. The box counting method can be used to obtain the fractal dimension of a wider range of fractal sets, and is usually the same as the similarity dimension. The fractal object is divided into boxes or fragments, and then counted and compared to the scale. The box dimension is defined [2]

$$D_B(F) = \lim_{r \rightarrow 0} \frac{\log N_r(F)}{-\log r}, \quad (1.1)$$

where D_B is the dimension of the fractal set F , N_r number of boxes required to cover the set, and r is the length of each box. This dimension is also called the capacity dimension of F [3].

The middle third Cantor set (Figure 1.2) is also a common example in fractal theory. We start with a line segment, and remove the middle third, and do the same operation on the remaining line segments. After infinitely many iterations, only Cantor “dust” remains. The length of the remaining segments, $(\frac{2}{3})^k$, converges to zero as $k \rightarrow \infty$. After k iterations, we have $N_k = 2^k$ line segments of length $\frac{1}{3^k}$. For $r \rightarrow 0$ we have that $k \rightarrow \infty$. Using Eq. (1.1) we find that $D_B(F) = \lim_{k \rightarrow \infty} \frac{\log 2^k}{-\log 3^{-k}} = \frac{\log 2}{\log 3} \approx 0.6309$. The Cantor set is an object with a dimension be-

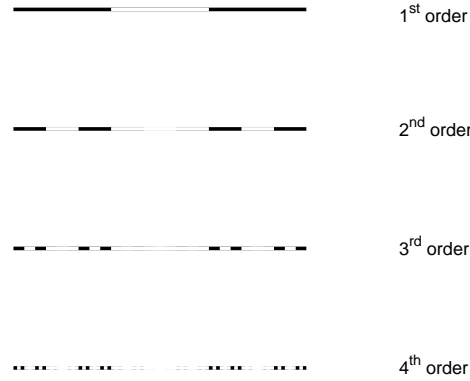


Figure 1.2: Cantor set carried to 4th order.

tween the dimension of a point and the dimension of a line.

Another way of characterizing a fractal, is finding the Hausdorff dimension. To define this dimension, we need to first define the Hausdorff measure. If $U \subset \mathbb{R}^n$, the diameter of U is defined as $|U| = \sup\{|x - y| : x, y \in U\}$. We say that $\{U_i\}$ is a δ -cover of F if $\{U_i\}$ is a countable collection of sets of diameter at most δ that cover F . If $F \subset \mathbb{R}^n$ and $s \geq 0$

$$H_\delta^s(F) = \inf \left\{ \sum_{i=1}^{\infty} |U_i|^s : \{U_i\} \text{ is a } \delta\text{-cover of } F \right\}, \quad (1.2)$$

for any $\delta > 0$. The s -dimensional Hausdorff measure of F is defined

$$H^s(F) = \lim_{\delta \rightarrow 0} H_\delta^s(F). \quad (1.3)$$

If the $H^s(F)$ is plotted against s , there will be a critical value where the graph “jumps” from ∞ to 0 [2]. This critical value is called the Hausdorff dimension of F .

$$D_H(F) = \inf\{s \geq 0 : H^s(F) = 0\} = \sup\{s : H^s(F) = \infty\}. \quad (1.4)$$

Again we can use the Cantor set as an example (Figure 1.2). The fractal set F can be divided into a left part $F_L = F \cap [0, \frac{1}{3}]$ and a right part $F_R = F \cap [\frac{2}{3}, 1]$. Both parts are geometrically similar to

F , but scaled by a ratio $\frac{1}{3}$, and $F = F_L \cup F_R$. We have that

$$H^s(F) = H^s(F_L) + H^s(F_R),$$

where $F_X = S(F)$, $X = L, R$ is a scaled version of F . If $\{U_i\}$ is a δ -cover of F , then $\{S(U_i)\}$ is a $\lambda\delta$ -cover of $S(F)$, and

$$\sum |S(U_i)|^s = \lambda^s \sum |U_i|^s,$$

$$H_{\lambda\delta}^s(S(F)) \leq \lambda^s H_\delta^s(F).$$

For the Cantor set we have

$$H^s(F_L) = H^s(F_R) = \left(\frac{1}{3}\right)^s H^s(F),$$

and

$$H^s(F) = \left(\frac{1}{3}\right)^s H^s(F) + \left(\frac{1}{3}\right)^s H^s(F) = 2 \left(\frac{1}{3}\right)^s H^s(F).$$

With $0 < H^s(F) < \infty$ (Falconer [2] proves that $\frac{1}{2} \leq H^s(F) \leq 1$) at the critical value $s = D_H$, we can divide by $H^s(F)$ and get

$$1 = 2 \left(\frac{1}{3}\right)^s, \quad \text{or} \quad s = \frac{\log 2}{\log 3}.$$

For the Cantor set $D_H = D_B$.

Chapter 2

Multifractals

The Koch curve and the Cantor set are examples of monofractals, which have only one dimension. Most fractals occurring in nature are multifractals, and may be considered as interwoven sets of fractals of different dimensions. These may be characterized by spectra of dimensions. Multifractal analysis has been applied to many fields, and different approaches have been used. The basic approaches may be divided into fine multifractal analysis and coarse multifractal analysis [2]. There are many parallels between the fine and the coarse approaches, and for many measures both approaches lead to the same multifractal spectra.

Both coarse and fine multifractal analysis make use of measures. A measure is a way of ascribing a numerical “size” to sets, such that if a set is decomposed into a countable number of pieces, then the size of the whole is the sum of the sizes of the pieces. We call μ a measure on \mathbb{R}^n if μ assigns a non-negative number to each subset of \mathbb{R}^n such that $\mu(\emptyset) = 0$, and $\mu(A) \leq \mu(B)$ if $A \subset B$. If A_1, A_2, \dots is a countable sequence of sets, then $\mu(\bigcup_{i=1}^{\infty} A_i) \leq \sum_{i=1}^{\infty} \mu(A_i)$, with equality if A_i are disjoint sets. The support of a measure is the set on which the measure is concentrated. The support $\text{spt}(\mu)$, is the smallest closed set X such that $\mu(\mathbb{R}^n \setminus X) = 0$, where $\mathbb{R}^n \setminus X$ is the complement of X . x is in the support if and only if $\mu(B(x, r)) > 0$ for all $r \geq 0$. For an attractor

$$\mu(A) = \lim_{m \rightarrow \infty} \frac{1}{m} \#\{k : 1 \leq k \leq m \text{ and } f^k(x) \in A\},$$

where $f : D \rightarrow D$ is a mapping on a domain D . A is a subset of D and $x \in D$ is some initial point. Thus, $\mu(A)$ represents the proportion of time that the iterates of x spends in A .

2.1 Coarse Multifractal Theory

The coarse approach is usually more practical when it comes to analysing physical examples or computer experiments. The irregularities of distribution of the measure μ of balls or cubes of radius r on \mathbb{R}^n is considered as $r \rightarrow 0$. This approach is related to the box counting dimension in Eq. (1.1). A way to characterize a multifractal is through the singularity spectrum, which in the coarse analysis is found from the relation

$$dN_r(\alpha) \sim r^{-f_C(\alpha)}, \quad (2.1)$$

where dN_r is the number of r -mesh cubes C such that $\mu(C) \sim r^\alpha$. More precisely we define the singularity spectrum as

$$f_C(\alpha) = \lim_{\varepsilon \rightarrow 0} \lim_{r \rightarrow 0} \frac{\log^+(N_r(\alpha + \varepsilon) - N_r(\alpha - \varepsilon))}{-\log r}, \quad (2.2)$$

where $\log^+ x \equiv \max\{0, \log x\}$, which ensures $f_C(\alpha) \geq 0$. $N_r(\alpha)$ is the number of r -mesh cubes with measure $\mu \geq r^\alpha$, and μ_i is the measure of the r -mesh cube i . Eq. (2.2) implies that if $\eta > 0$ and $\varepsilon > 0$ is small enough, then

$$r^{-f_C(\alpha) + \eta} \leq N_r(\alpha + \varepsilon) - N_r(\alpha - \varepsilon) \leq r^{-f_C(\alpha) - \eta} \quad (2.3)$$

for sufficiently small r .

The probability for a point to be in box i , p_i , is often rather used than the measure $\mu(C_i)$. We have that

$$p_i = \frac{\mu(C_i)}{\mu(\text{spt}(\mu))} = \frac{\int_{C_i} d\mu}{\int_{\text{spt}(\mu)} d\mu} \sim r^{\alpha_i}, \quad (2.4)$$

hence, p_i is a normalized measure, such that $\sum_i p_i = 1$.

$f_C(\alpha)$ is an exponent that measures how the number of r -mesh cubes with measure r^α scales as $r \rightarrow 0$. For different r these cubes can have different locations, so $f_C(\alpha)$ is a global characterization of the entire set, and is not the box dimension of the set of x such that $\mu(C(x, r)) \simeq r^\alpha$ as $r \rightarrow 0$ ($C(x, r)$ is the r -mesh cube containing x).

The singularity spectrum is also called the f - α curve, and I will use this term to refer to Eq. (2.2) to avoid confusion as I will introduce another spectrum used to characterize a multifractal, the generalized dimension spectrum [4]. To define the generalized dimension spectrum we define the q th power moment sum of p_i

$$M_q(r) = \sum p_i^q. \quad (2.5)$$

We find the generalized dimension through the relation

$$M_q(r) \sim r^{\tau(q)}, \quad (2.6)$$

with $\tau(q) = (q-1)D_q$, and then define D_q

$$D_q = \lim_{r \rightarrow 0} \frac{1}{q-1} \frac{\log M_q(r)}{\log r}. \quad (2.7)$$

With $q = 0$

$$\lim_{q \rightarrow 0} D_q = \lim_{r \rightarrow 0} -\frac{\log \sum p_i^0}{\log r} = \lim_{r \rightarrow 0} -\frac{\log N_r}{\log r}.$$

D_0 is the box dimension equivalent to Eq. (1.1). For $q = 1$ we Taylor expand the logarithm of the moment sum [5],

$$y(q) = \log \sum p_i^q.$$

The Taylor expansion near $q = 1$ is

$$y(q) = y(1) + \frac{dy}{dq}(q-1) + \dots = \sum p_i \log p_i.$$

We then have

$$D_1 = \lim_{r \rightarrow 0} \lim_{q \rightarrow 1} \frac{q-1}{q-1} \frac{\sum p_i \log p_i}{\log r} = \lim_{r \rightarrow 0} \frac{\sum p_i \log p_i}{\log r}. \quad (2.8)$$

The expression $-\sum p_i \log p_i$ is the information for a probability distribution [6], so D_1 is known as the information dimension. D_2 is equivalent to the correlation dimension [5]. To show this we

assume that the measure is represented by a finite set of points, and use the correlation sum

$$C(r) = \frac{1}{N(N-1)} \sum_{j=1}^N \sum_{i=j+1}^N \Theta(r - r_{ij}). \quad (2.9)$$

$\Theta(r)$ is the Heaviside function

$$\Theta(r) = \begin{cases} 0 & \text{if } r < 0 \\ 1 & \text{if } r \geq 0 \end{cases},$$

and r_{ij} is the distance between two points labeled i and j . We rewrite the moment sum

$$M_q(r) = \sum p_i p_i^{q-1}. \quad (2.10)$$

We rewrite the probability factor as $p_i \approx \frac{1}{N}$. For the other probability factor we use a better approximation, as the differences raised to power q will become more noticeable. We use Eq. (2.9) in Eq. (2.10)

$$p_j^{q-1} = \left[\frac{1}{N-1} \sum \Theta(r - r_{ij}) \right]^{q-1},$$

which gives the generalized correlation sum

$$C_q(r) = M_q(r) = \frac{1}{N} \sum_{j=1}^N \left[\frac{1}{N-1} \sum_{k=1, k \neq j}^N \Theta(r - r_{ij}) \right]^{q-1}. \quad (2.11)$$

One can then define the generalized dimension

$$D_q = \lim_{r \rightarrow 0} \frac{1}{q-1} \frac{\log C_q(r)}{\log(r)}. \quad (2.12)$$

For $q = 2$, Eq. (2.11) is the correlation sum, and D_2 is the correlation dimension. This is often a more preferred method computationally than using Eq. (2.7). D_1 is still defined as in Eq. (2.8)

D_q is connected to the f - α curve by Eq. (2.1) and Eq. (2.4). If we rewrite the sum to an integral in Eq. (2.5), we find that

$$M_q(r) = \sum p_i^q = \int p^q dN(\alpha, r) d\alpha \sim \int r^{q\alpha} r^{-f(\alpha)} d\alpha = \int r^{q\alpha - f(\alpha)} d\alpha. \quad (2.13)$$

As $r \rightarrow 0$, the integrand has a sharp peak when $q\alpha - f(\alpha)$ has its minimum. For each value of q there is a corresponding α_* such that

$$\left[\frac{d}{d\alpha} (q\alpha - f(\alpha)) \right]_{\alpha=\alpha_*} = 0,$$

and

$$\left[\frac{d^2}{d\alpha^2} (q\alpha - f(\alpha)) \right]_{\alpha=\alpha_*} > 0,$$

or equivalently

$$\left[\frac{d}{d\alpha} f(\alpha) = q \right]_{\alpha=\alpha_*}, \quad (2.14)$$

$$\left[\frac{d^2}{d\alpha^2} f(\alpha) < 0 \right]_{\alpha=\alpha_*}. \quad (2.15)$$

In the limit $r \rightarrow 0$, the value of the integral in Eq. (2.13) will then converge to

$$M_q(r) \sim r^{q\alpha_* - f(\alpha_*)}, \quad (2.16)$$

with $\alpha = \alpha_*$. We compare Eq. (2.16) with Eq. (2.5) and find that

$$\tau(q) = (q-1)D_q = q\alpha_* - f(\alpha_*) = \inf\{q\alpha - f(\alpha)\}, \quad (2.17)$$

which means that $\tau(q)$ is the Legendre transform of $f(\alpha)$, where $\tau(q) = (q-1)D_q$ [4].

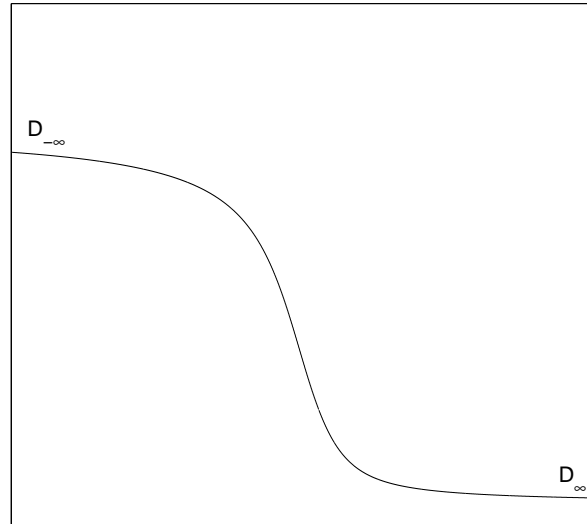
By differentiating $(q-1)D_q = q\alpha_* - f(\alpha_*)$ with respect to q we find that

$$\alpha_* = \frac{d}{dq} [(q-1)D_q], \quad (2.18)$$

and

$$f(\alpha_*) = q \frac{d}{dq} [(q-1)D_q] - (q-1)D_q. \quad (2.19)$$

Figure 2.1(a) shows the shape of a typical generalized dimension spectrum and Figure 2.1(b) shows the dimensions corresponding to the f - α curve. M_q (Eq. (2.5)) will be dominated by the



(a) Generalized dimension

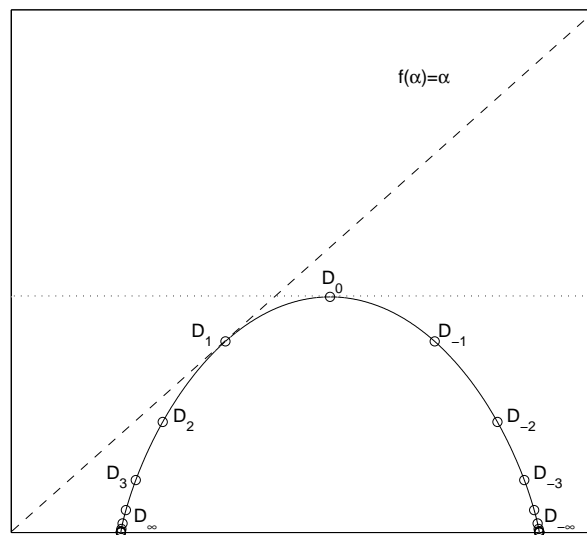
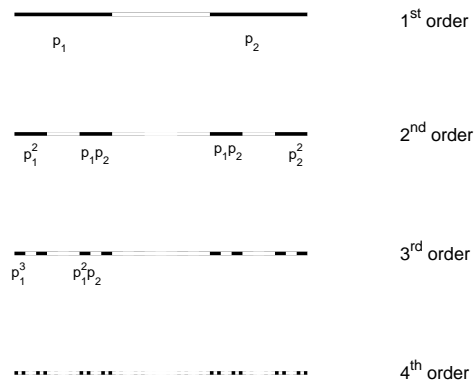
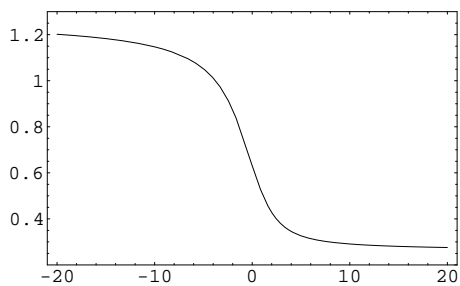
(b) f - α curve

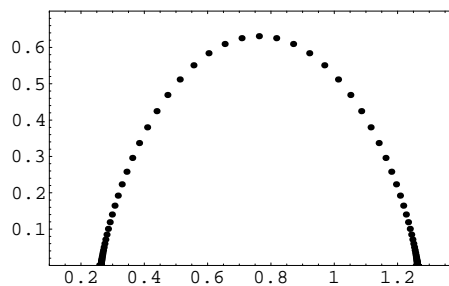
Figure 2.1: Shapes of typical multifractal spectra. The points D_q marked in (b) are the tangent points $\alpha_*(q)$ between the $f(\alpha)$ curve and the tangent line with slope q . This follows from Eq. (2.17).



(a) The weighted Cantor set



(b) Generalized dimension



(c) f - α curve

Figure 2.2: The weighted Cantor, and its spectra with $p_1 = 0.75$ and $p_2 = 0.25$.

largest probability value, p_{\max} , when $q \rightarrow \infty$, and $D_\infty \approx \lim_{r \rightarrow 0} \frac{\log p_{\max}}{\log r}$. When $q \rightarrow -\infty$, M_q will be dominated by the smallest probability value, p_{\min} , and $D_{-\infty} \approx \lim_{r \rightarrow 0} \frac{\log p_{\min}}{\log r}$. Since $p_i < 1$, D_q will have its smallest value when $q \rightarrow \infty$ and its largest value when $q \rightarrow -\infty$. In general $D_q \geq D_{q'}$ for $q < q'$. For monofractals $D_q = D_0$ for all q [5]. As shown in Figure 2.1, the f - α curve has its maximum in D_0 (this can easily be derived from Eq. (2.14) and Eq. (2.19)). The dashed line is the function $f(\alpha) = \alpha$, and is at tangent to the f - α curve in D_1 , so the information dimension is given by $D_1 = \alpha = f(\alpha)$ [7].

The weighted Cantor set (Figure 2.2(a)) is an example of a multifractal, and it is rather easy to follow the calculations for coarse analysis on this. We take a Cantor set with 2^k intervals of length $\frac{1}{3^k}$ at k th level as usual, but let the probability for a point to be in the left interval be p_1 and in the right interval to be p_2 , with $p_1, p_2 > 0$ and $p_1 + p_2 = 1$. For a regular Cantor

set $p_1 = p_2 = 0.5$. We have that a number $\binom{k}{r}$ of the k th level intervals of length r_k have mass $p_1^r p_2^{k-r}$, for instance at the 2nd level, we have $\binom{2}{2} = 1$ interval with mass p_1^2 , $\binom{2}{1} = 2$ intervals with mass $p_1 p_2$ and $\binom{2}{0} = 1$ interval with mass p_2^2 . We get that

$$M_q \left(\frac{1}{3^k} \right) = \sum_{r=0}^k \binom{k}{r} p_1^{qr} p_2^{q(k-r)} = (p_1^q + p_2^q)^k.$$

From Eq. (2.7), the generalized spectrum becomes

$$\begin{aligned} D_q(r) &= \lim_{r \rightarrow 0} \frac{1}{q-1} \frac{\log M_q(r)}{\log r} = \lim_{k \rightarrow \infty} \frac{1}{q-1} \frac{\log(p_1^q + p_2^q)^k}{\log \frac{1}{3^k}} \\ &= \lim_{k \rightarrow \infty} \frac{1}{q-1} \frac{k \log(p_1^q + p_2^q)}{k \log \frac{1}{3}} = \frac{1}{q-1} \frac{\log(p_1^q + p_2^q)}{\log \frac{1}{3}}. \end{aligned}$$

Using the Legendre transform we find α from Eq. (2.18)

$$\begin{aligned} \alpha &= \frac{d}{dq} [(q-1)D_q] = \frac{d}{dq} \frac{\log(p_1^q + p_2^q)}{\log \frac{1}{3}} \\ &= \frac{p_1^q \log p_1 + p_2^q \log p_2}{(p_1^q + p_2^q) \log \frac{1}{3}}, \end{aligned}$$

and $f(\alpha)$ from Eq. (2.19)

$$\begin{aligned} f(\alpha) &= q\alpha - (q-1)D_q \\ &= \frac{q(p_1^q \log p_1 + p_2^q \log p_2) - (p_1^q + p_2^q) \log(p_1^q + p_2^q)}{(p_1^q + p_2^q) \log \frac{1}{3}}. \end{aligned}$$

One can also find the f - α curve directly from Eq. (2.1) and Eq. (2.4), but this is more tedious, so the Legendre transform method is often more preferred.

For $p_1 = 0.75$ and $p_2 = 0.25$ we get the generalized dimension spectrum in Figure 2.2(b) and f - α curve in Figure 2.2(c). We see that the spectra has the typical shapes of multifractal spectra as discussed above.

2.2 Fine Multifractal Theory

In the fine approach to multifractals, we examine the structure and dimensions of the fractals that arise themselves. It parallels to finding the Hausdorff dimension of sets, and is more convenient for mathematical analysis.

First we define the local dimension, or Hölder dimension, of the measure μ at x by

$$D_{\text{loc}}(\mu(x)) = \lim_{r \rightarrow 0} \frac{\log \mu(B(x, r))}{\log r}, \quad (2.20)$$

where $B(x, r)$ is the local area of length r . For $\alpha \geq 0$ we define

$$F_\alpha = \{x \in \mathbb{R}^n : D_{\text{loc}}(\mu(x)) = \alpha\}. \quad (2.21)$$

The fine singularity spectrum or Hausdorff spectrum of μ is then defined

$$f_H(\alpha) = D_H(F_\alpha). \quad (2.22)$$

According to Falconer [2], we have that

$$\begin{aligned} D_H &\leq D_B \quad \text{and} \\ f_H(\alpha) &\leq f_C(\alpha). \end{aligned} \quad (2.23)$$

For self-similar measures we can define a quantity $\tau(q) = (q - 1)D_q$ playing a similar role in fine theory to that of Eq. (2.6) in coarse theory. The Legendre transform of $\tau(q)$ gives an upper bound for the fine multifractal spectrum, and in many cases gives the actual value.

A self-similar measure μ supported on a self-similar subset F of \mathbb{R} is considered. We let D be a closed subset of \mathbb{R}^n , and call a mapping $S : D \rightarrow D$ a contraction on D if there is a number c with $0 < c < 1$ such that $|S(x) - S(y)| \leq c|x - y|$ for all $x, y \in D$. With equality, S transforms sets into geometrically similar sets, and S is a contracting similarity. $S_1, \dots, S_m : \mathbb{R} \rightarrow \mathbb{R}$ are contracting similarities with ratios c_1, \dots, c_m , and p_1, \dots, p_m are probabilities as defined in Eq. (2.4). $\tau(q)$ is then defined as the positive number satisfying

$$\sum_{i=1}^m p_i^q c_i^{-\tau(q)} = 1. \quad (2.24)$$

Differentiating Eq. (2.24) with respect to q gives

$$\sum_{i=1}^m p_i^q c_i^{-\tau(q)} \left(\log p_i - \frac{d\tau}{dq} \log c_i \right) = 0, \quad (2.25)$$

and differentiating again gives

$$\sum_{i=1}^m p_i^q c_i^{\tau(q)} \left(\left(\log p_i - \frac{d\tau}{dq} \log c_i \right)^2 - \frac{d^2\tau}{dq^2} \log c_i \right) = 0 \quad (2.26)$$

Since $\log c_i < 0$ ($c_i \rightarrow 0$), it follows that $\frac{d^2\tau}{dq^2} \leq 0$, so $\tau(q)$ is concave in q , and then that there is a range of $\alpha \in [\alpha_{\min}, \alpha_{\max}]$ for which the graph of τ has a line of support L_α of slope $-\alpha$. For such α this support line is unique, and the Legendre transform of τ is $f : [\alpha_{\min}, \alpha_{\max}] \rightarrow \mathbb{R}$ given by the value of the intercept of L_α with the vertical axis. f is continuous in α . The fine, or Hausdorff, multifractal spectrum is the Legendre transform of $\tau(q)$ for self-similar multifractals [2],

$$f(\alpha) = \inf\{\alpha q - \tau(q)\}. \quad (2.27)$$

For a given α , the infimum in Eq. (2.27) is attained at a unique q . By differentiating $q\alpha - \tau(q)$ we find that

$$\alpha = \frac{d}{dq} \tau(q), \quad (2.28)$$

and

$$f(\alpha) = q \frac{d}{dq} \tau(q) - \tau(q), \quad (2.29)$$

similar to what obtained for the coarse theory. Again $f(\alpha)$ has its maximum in D_0 , and $D_1 = \alpha = f(\alpha)$ [2].

To illustrate the fine theory, we can again look at the weighted Cantor set. Using $p_i = \binom{m}{i} p_1^i p_2^{m-i}$, we find $\tau(q)$ through Eq. (2.24),

$$\begin{aligned} \sum_{i=1}^m p_i^q c_i^{-\tau(q)} &= \sum_{i=1}^m \binom{m}{i} p_1^{qi} p_2^{q(m-i)} \left(\frac{1}{3} \right)^{-m\tau(q)} \\ &= (p_1^q + p_2^q)^m \left(\frac{1}{3} \right)^{-m\tau(q)} = 1. \end{aligned}$$

$$\begin{aligned} \left(\frac{1}{3}\right)^{-m\tau(q)} &= (p_1^q + p_2^q)^{-m} \\ -m\tau(q) &= \frac{-m \log(p_1^q + p_2^q)}{\log \frac{1}{3}} \\ \tau(q) &= \frac{\log(p_1^q + p_2^q)}{\log \frac{1}{3}}. \end{aligned}$$

We can then use Eq. (2.28) and Eq. (2.29) to find that

$$\begin{aligned} \alpha &= \frac{p_1^q \log p_1 + p_2^q \log p_2}{(p_1^q + p_2^q) \log \frac{1}{3}} \quad \text{and} \\ f(\alpha) &= \frac{q(p_1^q \log p_1 + p_2^q \log p_2) - (p_1^q + p_2^q) \log(p_1^q + p_2^q)}{(p_1^q + p_2^q) \log \frac{1}{3}}, \end{aligned}$$

as for the coarse theory.

2.3 Multifractal Time Series

When analysing real data, we often work with time series. We must then take time dependency into account when we do multifractal analysis. Instead of dividing the set into boxes and finding the measure within each box, we define a local measure using the derivative of the time series [8].

$$\mu_A = \int_A d\tau |x'(\tau)|, \quad (2.30)$$

where A is the local area, x is the time series in question and $x'(t)$ the derivative with respect to time. For a discrete time series we define the measure

$$\mu_A = \sum_A |\Delta x(t)|, \quad (2.31)$$

where $\Delta x(t)$ denotes the differentiated time series. We can then define a partition function [9] similar to the moment function, Eq. (2.5).

$$Z_q(\Delta t) = \sum_i \mu([t_i, t_i + \Delta t])^q \sim \Delta t^{\tau_q}, \quad (2.32)$$

where $\tau_q = (q - 1)D_q$. We find the generalized dimension spectrum from Eq. (2.32), and the f - α -curve using the Legendre transform.

2.3.1 Wavelet Transform Modulus Maxima

When applying multifractal analysis to time series, the wavelet transform modulus maxima method (WTMM) has proven to be a powerful tool in characterising the scaling properties of multifractal measures [10], and especially for non-stationary time series ([11], references therein). Different authors have used somewhat different methods applying the wavelet transform to multifractal analysis. Turiel [8] uses the wavelet transform of the differentiated time series,

$$T_\Psi(\Delta t, t) = \frac{1}{\Delta t} \sum_{t'=1}^N |\Delta x|(t') \Psi\left(\frac{t-t'}{\Delta t}\right), \quad (2.33)$$

while Oświęcimka uses the wavelet transform of the original time series,

$$T_\Psi(\Delta t, t) = \frac{1}{\Delta t} \sum_{t'=1}^N \Psi\left(\frac{t'-t}{\Delta t}\right) x(t'), \quad (2.34)$$

where Δt is a scale parameter and a measure of the width of the wavelet, and t the time parameter where the wavelet is centered. N is the total amount of points in the time series. ψ is the analysing wavelet, and should be well localised in both space and frequency. ψ must be of zero mean, should be orthogonal to some loworder polynomials for the purpose of singularity tracking. The most commonly used family of wavelets in multifractal analysis, is the m th derivative of the Gaussian function [9]

$$\psi^{(m)}(x) = \frac{d^m}{dx^m}(e^{-x^2/2}). \quad (2.35)$$

This wavelet removes the signal trends that can be approximated by polynomials up to $(m - 1)$ th order. In the presence of singularities in data one observes the power-law behaviour of the coefficients T_ψ ,

$$T_\psi(\Delta t, t) \sim \Delta t^{\alpha(t)}. \quad (2.36)$$

We define the fractal component F_α associated to the singularity exponent α as

$$F_\alpha = \{t : \alpha(t) = \alpha\}. \quad (2.37)$$

The singularity spectrum, $f(\alpha)$ is then defined as the Hausdorff dimension of F_α [8]. This method is similar to the fine multifractal theory.

According to [11] this relation is not stable in the case of densely packed singularities. A better method is to identify the local maxima of T_ψ and then calculate the partition function from moduli of the maxima

$$Z_q(\Delta t) = \sum_{l \in \mathcal{L}(\Delta t)} \sup \{|T_\psi(\Delta t', t_l(\Delta t'))|\}^q \sim \Delta t^{\tau_q}, \quad (2.38)$$

where t_l is the position of a maxima line, l , contained in the set of maxima lines $\mathcal{L}(\Delta t)$ for a given scale Δt . This method is similar to the coarse analysis method, where the analysing wavelet ψ can be seen as a box of a particular shape, and the scale Δt its size, like r in Eq. (2.5). The modulus maxima indicate how to position the “boxes” to obtain a partition at the considered scale [9].

2.3.2 Multifractal Detrended Fluctuation Analysis

The detrended fluctuation analysis (MFDFA) has become a commonly used tool in analysis of scaling properties of monofractal signals and in identifying correlations present in noisy nonstationary time series ([11], references therein). The multifractal generalization of this procedure can be sketched as follows. First the integrated signal profile $Y(j)$,

$$Y(j) = \sum_{i=1}^j (x(i) - \langle x \rangle), \quad j = 1, \dots, N, \quad (2.39)$$

where $\langle \dots \rangle$ denotes averaging over the time series, $x(i)$, and then one divides it into M_n segments of length $n < N$, N is the total number of points, starting from both the beginning and the end of the time series (i.e., $2M_n$ such segments in total). Each segment v has its own local trend that can be approximated by fitting an l th order polynomial $P_v^{(l)}$ and subtracted from the data. The variances for all the segments v and all segment lengths n must then be evaluated,

$$F^2(v, n) = \frac{1}{n} \sum_{j=1}^n \{Y[(v-1)n+j] - P_v^{(l)}(j)\}^2. \quad (2.40)$$

$F^2(v, n)$ is averaged over v 's and the q th-order fluctuation function is calculated for all possible segment lengths n

$$F_q(n) = \left(\frac{1}{2M_n} \sum_{v=1}^{2M_n} [F^2(v, n)]^{q/2} \right)^{1/q}. \quad (2.41)$$

$F_q(n)$ reveals power-law scaling within a significant range of n ,

$$F_q(n) \sim n^{h(q)}. \quad (2.42)$$

A family of generalized Hurst exponents, $h(q)$, is found, and the f - α curve calculated using the relation

$$\alpha = h(q) + qh'(q), \quad (2.43)$$

$$f(\alpha) = q[\alpha - h(q)] + 1. \quad (2.44)$$

Chapter 3

A Random Walk Through Applications of Multifractals in Science

Objects of multifractal character have been studied in a diversity of research fields. Naturally, there are abundant fractal phenomena in geology, where the concept was first introduced. After its introduction, other sciences have found their use of fractals as well, for instance other natural sciences, like space physics, biology and chemistry, but also medicine and finance. The fractals mentioned in Chapter 1, the Koch curve and the Cantor set, are deterministic fractals. Natural fractals are statistical; there will be statistical fluctuations in the measure of fractality, and the perimeter of the fractal will be statistical. For instance, a natural fractal could be similar to a Cantor set where a third of the line segment is removed at random. The fractal would have the same fractal dimension as the deterministic Cantor set, but not look the same, and no longer be deterministic. Also, natural fractals are not scale invariant for all scales like deterministic fractals. Thus, it is meaningless to take the limit $r \rightarrow 0$ when calculating fractal dimensions for natural fractals. For physical examples, the estimates of dimensions will break down well before a molecular scale is reached [2]. Still, fractal analysis can be applied on numerous objects, and deterministic fractals can often be used as models for natural fractals within a certain range of scales, limited by the properties of the object, for instance the range of sizes a rock may have.

3.1 Geology

As mentioned in chapter 1, a rocky coastline is fractal. There is a great number of other monofractal phenomena in geology, like sediment deposition and rock fragmentation [1], but also a lot of structures with multifractal properties. De Wijs multiplicative cascade (Figure 3.1)

ϕ_2		$(2-\phi_2)$		
ϕ_2^2	$\phi_2(2-\phi_2)$		$(2-\phi_2)^2$	
ϕ_2^3	$\phi_2^2(2-\phi_2)$	$\phi_2(2-\phi_2)^2$		$(2-\phi_2)^3$
ϕ_2^4	$\phi_2^3(2-\phi_2)$	$\phi_2^2(2-\phi_2)^2$	$\phi_2(2-\phi_2)^3$	$(2-\phi_2)^4$

Figure 3.1: De Wijs multiplicative cascade carried to 4th order.

is a model for mineral concentration [1]. In this model an original mass of rock is divided into two equal parts with equal mass. The original mass of the rock has a mean mineral concentration C_0 , which is the ratio of the mass of mineral to mass of rock. It is hypothesized that the mineral is concentrated into one of the two elements such that one element is enriched and the other is depleted. The mean mineral concentration in the enriched element C_{11} is given by $C_{11} = \phi_2 C_0$, where ϕ_2 is the enrichment factor. The depleted element must then be $C_{12} = (2 - \phi_2)C_0$ for mass balance, and the enrichment factor must be in the range $1 < \phi_2 < 2$. The process of concentration is then repeated at the next order as illustrated in Figure 3.1. Using Eq. (2.5) and Eq. (2.7) the generalized dimension for De Wijs multiplicative cascade is found to be

$$D_q = -\frac{1}{(q-1)\log 2} \log \left[\left(\frac{1}{2}\phi_2 \right)^q + \left(1 - \frac{1}{2}\phi_2 \right)^q \right].$$

For $q = 1$ Eq. (2.8) is used to find

$$D_1 = -\frac{1}{\log 2} \left[\frac{1}{2}\phi_2 \log \left(\frac{1}{2}\phi_2 \right) + \left(1 - \frac{1}{2}\phi_2 \right) \log \left(1 - \frac{1}{2}\phi_2 \right) \right].$$

De Wijs multiplicative cascade is a perfect multifractal for all values of q .

Spatial distribution of seismicity has for a long time been known to have a self-similar fractal structure, and spatial clustering of seismic activity may be used for earthquake prediction [1],[12]. A multifractal approach to the investigation of earthquakes has shown that the multifractal spectra gives information about intensities of seismicity at particular sites. In [12] the

seismic regions in Pamir-Tyan Shan, Caucasus and California was studied and the multifractal analysis revealed a self-similar hierarchical structure of seismicity and a non-trivial spectrum of singularity indices. The spectra contained information about the fine structure of seismicity; spatial intermittence of seismicity as well as patches of concentrated and rarefied seismic activity.

3.2 Space Physics

Solar wind turbulence is believed to be multifractal. Scaling properties of the energy flux of the turbulent kinetic energy in the solar wind have been studied, using the energy flux near the dissipation range at the proton gyro scale to estimate the dissipation field [13]. The data used was obtained by the Helios 2 solar probe during its first perihelion passage in 1976, where high-speed solar wind data was prioritised. The analysis showed a multifractal nature of the dissipation field, and revealed that intermittence prevails, and that the set of points in real physical space supporting the dissipation field had a multifractal structure. The f - α curve was estimated for the first time for MHD turbulence in the solar wind by Marsch et al. [13], and its features resembled those obtained for turbulent fluids. A p-model introduced by Meneveau and Sreenivasan [14] was compared with the real data. In this model the flux of kinetic energy to smaller scales is randomly divided at each step into nonequal reactions p_1 and p_2 , with $p_1 + p_2 = 1$. The generalized dimension spectrum for this model is given

$$D_q = \frac{1}{q-1} \frac{\log(p_1^q + p_2^q)}{\log 2}.$$

The real data had a good fit with $p_1 = 0.87$, indicating a strongly intermittent multifractal energy cascade.

The interplanetary magnetic field (IMF) also shows multifractal structure. The multifractal character of the magnetic field strength fluctuations generalizes the concept that the magnetic field is organised into interaction regions and rarefaction regions. Near solar maximum the interaction regions in the distant heliosphere might be viewed as clusters of strong disturbed fields with considerable fine structure on various scales [15]. Large-scale fluctuations of the IMF are defined loosely as the fluctuations of the magnetic field on scales from several hours to the solar rotation period, ~ 26 days. Fractal behavior of the large-scale fluctuations of the magnetic field strength was observed in 1987 by Burlaga and Mish ([15], references therein), but it was later found that there is an existence of multifractal structure. The multifractal concept considers higher mo-

ments of the magnetic field, which are important when the magnetic field distribution has a large tail and when the fluctuations in the magnetic field are comparable to or larger than the mean field. Such is the case of the IMF strengths distribution. Burlaga analysed the IMF observed by Voyager 2 near 25 AU, 1987-1988 [15], and found that the shape of the f - α curve was similar to that obtained from fully developed turbulence, studied by for instance Meneveau and Sreenivasan [14]. The multifractal properties was found over scales from 16 hours to 21 days.

Another example in this context, is turbulence in the magnetospheric cusp. At the magnetopause near the polar cusp there is a region that is characterized by strong and persistent magnetic turbulence known as the turbulent boundary layer. This turbulence could be very important for the mass transport into the cusp, and may cause acceleration and heating of plasma. Fluctuations at different frequencies form wave trains suggesting multiscale, intermittent processes operating in the turbulent boundary layer ([16], references therein). Yordanova et al. [16] have studied data from NASA Polar satellite, measured in the northern cusp region at distance 3-4 Earth radii to the reference magnetopause. They found a non-linear behavior interpreted as an intermittence phenomenon and as a direct consequence of the existence of spatial fluctuations in the local regularity of the velocity field. This behavior showed multifractality, corresponding to different types of turbulence depending on the direction of the IMF. For northward IMF conditions the turbulence was consistent with the previously mentioned p-model of fully developed fluid turbulence. For southward IMF the data agreed with a model of non-fully developed Kolmogorov-like fluid turbulence [16].

3.3 Biology

Fractals have a wide range of applicability in biology too. Trees, shrubs and smaller plants like ferns have a repeating structure over a range of scales, and we can see that they have quite obvious fractal properties just by looking at them. An example of a multifractal system in biology is the gap formation in rainforests. Treefall, gap formation and regeneration have been shown to be a major force in tropical ecosystems. When trees have grown old, they fall down and leave a gap in the canopy, giving new plants the chance to develop. The opening of a gap shakes the forest equilibrium to the starting point and recurrent successional phases are observed. In this way, gaps contribute to the maintenance of high diversity levels in tropical rainforests ([17], references therein). Solé and Manrubia have studied the Barro Colorado Island forest, a remnant of rainforest isolated after the formation of the Panama Canal, and found that the spatial structure of

gaps is multifractal [17]. They also found that a simple cellular automata model can account for some relevant part of the complexity of a rainforest when gap dynamics is present. The system is self-organized, meaning that before the system reaches a critical state, it does something to avoid this, in this example a tree will fall. The gap size will be proportional to the size of the dying tree and the gap formation is multifractal.

The cellular automata model is a mathematical model for complex natural systems with local interactions, and the value of each automaton is determined by the previous values of a neighbourhood of sites around it. A square grid with $L \times L$ points is considered. An automaton is placed in a grid cell and behaves according to rules determined by the system considered. A simple example of cellular automata is the sandpile model, where sand particles are the automata [1]. In the rain forest example, the automata are the trees starting to grow in a given cell. A given tree will grow if the screening from the nearest trees is weak enough, and it will grow at a given rate. A given tree will die randomly with a certain probability and treefall will take place. No trees beyond a specified size can exist, so if a tree grows beyond this size, it will fall too. A new tree can appear at any empty grid cell with a certain probability, and the size of the new tree is the smallest one. A canopy gap will be formed each time a tree dies and the gap size will be proportional to the size of the tree. A gap formation with a multifractal structure will be formed.

3.4 Chemistry

In chemistry, multifractality is found in some non-linear chemical reactions in self-organizing systems [18]. In a study of properties of copper sulfide film [19], the process of growth in the film was found to be organized in three parts. It was the growth of fractal films of copper sulfide formed during the oxidation of ascorbic acid by aerial oxygen in the presence of a copper coordination compound and sodium sulfide that was studied. At the first stage of growth, the structure became less multifractal and more uniform, as the formation of the films occurred as a result of formation of new growth centers. In the next stage the films were characterized by a box dimension value that indicated that the films were growing in accordance with diffusion limited aggregation mechanism (this will be explained later in this section), and at the same time there was an increase in fractal divergence into a wide range of fractal dimensionality, leading to a formation of multifractal films with high fractal divergences. In the last stage the constant values of fractal dimensionality and the characteristics of the multifractal spectrum indicated that growth had ceased. The experiment showed that multifractal analysis has to be performed for a

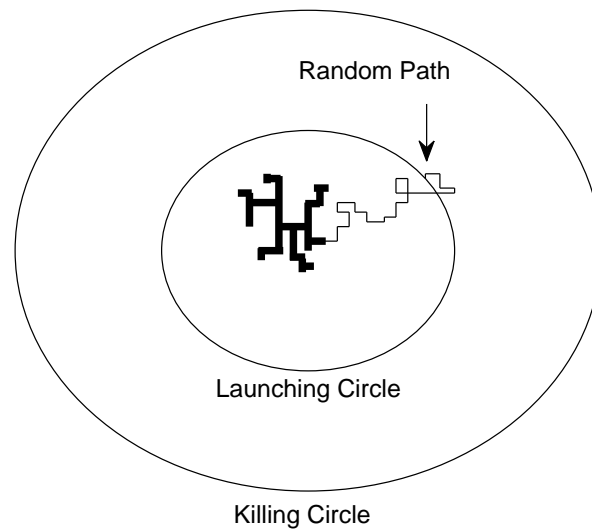


Figure 3.2: Illustration of DLA growth of a cluster. An accreting cell is introduced at a random point on the “Launching Circle” and carries out a random walk until it accretes to the growing cluster (or crosses the “Killing Circle”).

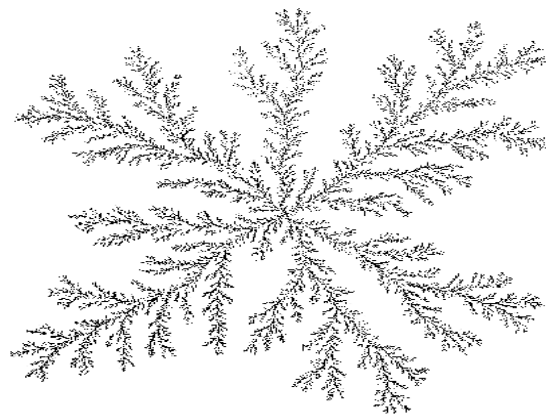


Figure 3.3: Illustration of a fractal structure created by DLA.

sufficient description of the properties of the films, and that the influence of multifractal characteristics can be transferred to similar chemical reactions.

Diffusion limited aggregation (DLA) is a concept used to model for instance fractal growth or drainage networks [1]. It was introduced by Witten and Sander in 1981 [20]. A two-dimensional grid of cells is considered, and a seed cell is placed near the center of the grid. An accreting cell is introduced on a “launching circle” and follows a random path until it either accretes to the growing cluster of cells by entering a cell adjacent to the cluster, or wanders across a “killing circle” in which a new cell is introduced on the “launching circle” (Figure 3.2). The result is a sparse dendritic structure (Figure 3.3), because the random walkers are more likely to accrete near the tips of the cluster rather than the deep interior.

3.5 Medicine

Many physiological time series are extremely inhomogeneous and non-stationary, fluctuating in an irregular and complex manner [21]. Analysis of the human heart rate [21], [22] indicate that the heart rate of healthy humans is a multifractal signal. In [21] recordings from both daytime and nighttime have been performed, so the multifractality of healthy heartbeat dynamics cannot be explained by activity nor sleep-stage transition. Heart-rate data from subjects with congestive heart failure have a clear loss of multifractality. The f - α spectrum is very narrow, indicating monofractal behaviour. An analysis incorporating the multifractal method may add diagnostic power to contemporary analytic methods of heartbeat time series analysis. The change in shape for the f - α curve for the heart-failure group may provide insight into the changes in the cardiac control mechanisms resulting from this pathology.

3.6 Finance

According to Turiel and Pérez-Vicente [8], multifractal analysis has proven to be a very powerful method to deal with and interpret economical data. Many self-organized systems that exhibit properties of scale invariance can well describe stock markets and other socio-economical systems. In [8] data from stock markets have been analysed and found to be multifractal, and also reconstructable. Simple models of stock prices can be represented by realizations of Brownian motion or fractional Brownian motion [2]. A more sophisticated approach uses multifractal time, where the prices follow Brownian or fractional Brownian motion, but with respect to rescaled

time called trading time [2]. Financial time series makes a good source for multifractal analysis, as many economic indices have been recorded more or less continuously for a long time, sometimes hundreds of years. Therefore it might be interesting for all kinds of scientists to investigate these time series, finding the most accurate method for multifractal analysis.

Chapter 4

Data Analysis

I have analysed the activity signal of a Bak-Tang-Wiesenfeld sandpile model to check if I had implemented the equations for multifractal analysis correctly, to check the accuracy of the analysis method and to get spectra to compare with those obtained for other data. I have analysed the interplanetary magnetic field strength, the AE index and the D_{st} index.

The IMF data analysed is downloaded from NASA's Coordinated Data Analysis Web [23]. I have used 1 AU 1-minute resolution IMF data. The data are provided by four spacecrafts, and time-shifted to the Earth's bow shock nose. Time shifting is based on the assumption that solar wind magnetic field values observed by a spacecraft at a given time and place lie on a planar surface convecting with the solar wind, and that the same values will be seen at different places at the time when the phase front sweeps over that location. Four shift techniques are used, described in [24]. The following spacecrafts have provided the data:

ACE (Advanced Composition Explorer) was launched August 25, 1997, and continues to provide magnetic field, plasma and energetic particle data from a ~ 180 day L_1 orbit having X , Y , and Z (Geosentric Solar Ecliptic coordinates) ranges of 220 to 250 R_E (Earth radii), -40 to +40 R_E , and -24 to +24 R_E . For the Geosentric Solar Ecliptic system, GSE, X points to the Sun, Z points northward and normal to the ecliptic plane (the plane of the Earth's orbit). The ACE home page is at <http://www.srl.caltech.edu/ACE/>.

Wind was launched November 1, 1994, as part of NASA's contribution to the International Solar Terrestrial Program. It continues to obtain magnetic field, plasma, energetic particle and plasma wave data. Since mid-2004, it has been in an L_1 orbit with excursions in Y (GSE) between $\pm 100 R_E$. It had multiple earlier phases, including an interval spanning the last third of 2000 through mid 2002 with Y (GSE) excursions in excess of 200 R_E and an interval in late 2003 and early

2004 in orbit about the Lagrange point¹ on the anti-sunward side of Earth. The Wind home page is at <http://pwg.gsfc.nasa.gov/wind.shtml>.

IMP 8 was launched October 26, 1973, into a low eccentricity Earth orbit. Apogee and perigee distances have been in the ranges 38-45 R_E and 28-34 R_E . On average IMP 8 is out of the solar wind for about 5 days of every 12.5 day orbit. The IMP 8 web page is at

<http://nssdc.gsfc.nasa.gov/space/imp-8.html>.

Geotail was launched July 24, 1992, into an eccentric orbit with apogee deep in the geotail. In early 1995, the Geotail orbit was adjusted to about $10 \times 30 R_E$, and then to $9 \times 30 R_E$ in 1997 where it continues today (2008). In this orbit, Geotail has annual solar wind “seasons” with apogee local times on or near the Earth’s dayside, and it has solar wind intervals during each ~ 5 day orbit of the solar wind seasons.

The datafiles available for downloading contains many parameters connected to IMF and plasma data. I chose to extract the data for the values of the magnetic field, B_x , B_y and B_z in the geocentric solar-magnetospheric system, all 1-minute data in nT.

The data AE index data and the D_{st} index data analysed are downloaded from the Kyoto database [26]. The AE index data is taken at 12 observatories. The stations are in Abisko, Dixon Island, Cape Chelyuskin, Tixie Bay, Cape Wellen, Barrow, College, Yellowknife, Fort Churchill, Poste-de-la-Baleine, Narsarsuaq and Leirvogur. For the derivation of the D_{st} index, four magnetic observatories are used. These are in Hermanus, Kakioka, Honolulu and San Juan.

¹The Lagrange points are five points fixed within the rotating frame of reference at which a stationary body will be in equilibrium. Denoted by L_1 to L_5 , they all lie in the plane defined by the orbits of the primary bodies around each other. L_1 , L_2 and L_3 lie on the line joining the primary bodies, and correspond to unstable equilibrium positions. In the Earth-Sun system, L_1 is the point on a line between the Earth and the Sun where the gravity force from each of the bodies is equal. L_2 lies on the extension of this line on the nightside of the Earth where the gravitational forces of the two bodies balance the centrifugal force on the the smaller mass [25].

4.1 Sandpile

The Bak-Tang-Wiesenfeld (BTW) sandpile model is a dynamical system displaying self-organized criticality. It is named after Per Bak, Chao Tang and Kurt Wiesenfeld. A “pile of sand” is build by randomly adding sand, a grain at a time. The pile will grow, and the slope will increase. One hypothesis for the behaviour of the sand pile is that grains could be added until the slope is everywhere at an angle of repose. Eventually, the sandpile would reach a critical state, and if more sand is added, it will would slide off. But this is not what happens. As the critical state is approached additional sand grains trigger landslides of various sizes. The frequency-size distribution of landslides is fractal. The sandpile is said to be in a state of self-organized criticality [27], [1].

For the BTW sandpile, the dynamics in two dimensions are as follows:

$$\begin{aligned} z(x-1, y) &\rightarrow z(x-1, y) - 1, \\ z(x, y-1) &\rightarrow z(x, y-1) - 1, \\ z(x, y) &\rightarrow z(x, y) + 2, \end{aligned} \tag{4.1}$$

and

$$\begin{aligned} z(x, y) &\rightarrow z(x, y) - 4, \\ z(x, y \pm 1) &\rightarrow z(x, y \pm 1) + 1, \\ z(x \pm 1, y) &\rightarrow z(x \pm 1, y) + 1 \text{ for } z(x, y) > z_c, \end{aligned} \tag{4.2}$$

where we have the square array (x, y) , for $1 \leq x, y \leq N$. The sand columns are represented by the bonds between nearest neighbours in the x and y direction, and $z(x, y)$ represents the average slope in the diagonal direction. Eq. (4.1) represent the addition of two units at the upper and left bonds. Eq. (4.2) represent two units of sand, located at the left and upper bonds at (x, y) sliding in the diagonal direction to the right and lower bonds. When $z > z_c$, one unit of sand slides in the x direction and one in the y direction. The resulting dynamics will involve next-nearest-neighbour interaction with the basic physics unchanged. In principle, the slope in 2D is a vector field, but the scalar field z is easier to work with, and these rules incorporate the essential physics involved. The system will become stable at the point when the network of minimally stable clusters has been broken down to the level where the activity signal cannot be communicated through infinite distances. At this point there will be no length scale, and, consequently, no time scale. After

reaching the critical state the activity signal is monofractal in time [27].

I have analysed the activity signal of a 64×64 BTW sandpile model. The implemented code is described in the Results section, and the Mathematica notebook used for the analysis is to be found in Appendix A-1. The implementation of the generation of the signal analysed is done by Martin Rypdal, and the notebook is to be found in Appendix A-2.

Figure 4.1 shows the spectra for the activity signal. For a monofractal the generalized di-

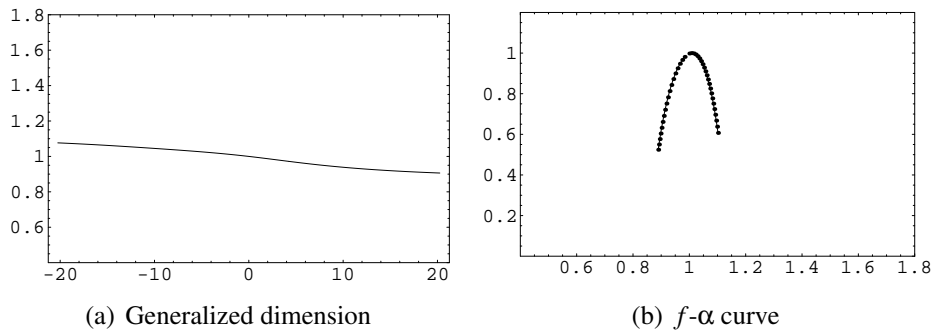


Figure 4.1: Spectra for the BTW sandpile model, using scales from $2^6 - 2^{18}$

mension is independent of q and is a straight line in the box dimension. The f - α curve vanishes except for one value of α . For a discrete time series where $\Delta x(t) \neq 0$ at all times, the box dimension must be $D_B = D_0 = 1$. Since the maximum of the f - α curve corresponds to $q = 0$, we have from Eq. (2.19) that $f(\alpha_*) = D_0 = 1$ at this point, and from Eq. (2.18) we have $\alpha_* = D_0 - \left[\frac{dD_q}{dq} \right]_{q=0} = 1 + \left| \frac{dD_q}{dq} \right|_{q=0}$. For a monofractal $\frac{dD_q}{dq} = 0$ and hence $\alpha_* = 1$. As we can see from Figure 4.1(a) the generalized dimension is not entirely independent of q when using scales from $2^6 - 2^{18}$. Knowing that the signal is monofractal, this seems to be due to the method used for analysing. The discrepancy from the actual generalized dimension is larger as $|q| \rightarrow \infty$, especially for $q \ll 0$. According to [11] this is also the case for the wavelet transform modulus maxima method, and there is no simple and straightforward explanation of why that is. Looking at the f - α curve in Figure 4.1(b), $f(\alpha)$ is not centered in one point as it should be for a monofractal. However, most of the points are in the value of α corresponding to the monofractal dimension, and for a multifractal more points are found in the region where $|q| \rightarrow \infty$, as shown in Figure 2.1(b). It seems like the spectrum “leaks” out on the sides when $|q| \rightarrow \infty$. However, when using larger scales, the spectra look more monofractal. Figure 4.2 shows the spectra when using scales from $2^{12} - 2^{18}$, and now the generalized dimension is almost a perfectly straight line in the box dimension. The “leakage” in the f - α curve is much smaller, so it seems that we get more

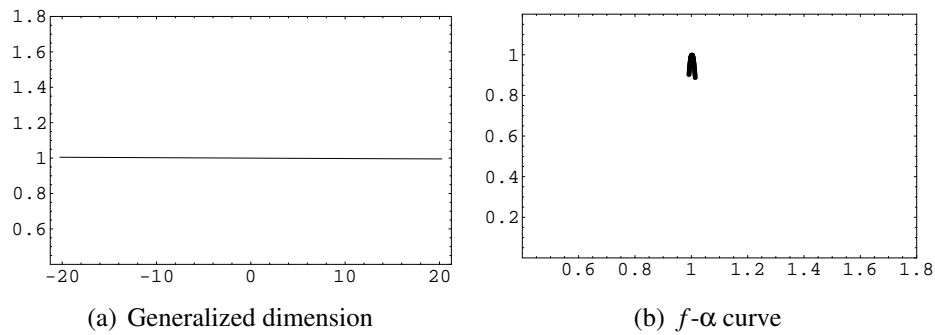


Figure 4.2: Spectra for the BTW sandpile model, using scales from $2^{12} - 2^{18}$

accurate results using larger scales. A white noise time series have been analysed with the same code, with the same results. Using shorter scales gave inaccurate results, but using scales from $2^{12} - 2^{18}$, the generalized dimension spectrum was a perfectly straight line in the box dimension, and the f - α curve vanished except from one point. The analysis method used gives very accurate results for the generated time series when the time series have a large enough amount of points, and only larger scales are used.

4.2 The Interplanetary Magnetic Field

The interplanetary magnetic field (IMF) mentioned in section 3.2 has a central role in many examples on multifractality in space physics. The IMF is the field associated with the solar wind. The solar wind is the moving plasma of ionized particles and associated magnetic fields that are expanding outward from the Sun. The wind exists out past 150 AU because the pressure of the interstellar medium is insufficient to confine the energetic particles coming from the hot solar corona. This solar-wind dominated region is the heliosphere [28].

The solar wind particles themselves are moving radially from the Sun, but the rotation of the emitting solar surface about an axis that is nearly perpendicular to the ecliptic plane provides a spiral flow pattern for the particle density and its associated fields. This phenomenon is often referred to as the “garden hose effect”, since water from a rotating garden sprinkler will flow in such a spiral pattern. It is also known as an Archimedes spiral. At 1 AU the angle between the field and a line drawn from the Sun is close to 45° .

The IMF is said to be frozen into the the solar wind plasma, meaning that the magnetic flux through a surface remains constant even as the surface changes location and shape. The field lines that penetrate the surface is being held in place so tightly that as the surface stretches or shrinks, the field lines will move apart or move closer together. The field will be weakened or strengthened, but the combination of changed magnetic field strength and changed area of the surface leaves the flux unchanged [29]. The reason for the IMF to be a frozen-in field is that the magnetic field is weak in the solar wind, so the combined motion of the solar wind particles in the magnetic field drags along the field itself. The solar-wind electrical conductivity is so large that the wind can be considered a perfect conductor. A perfect conductor moving in a magnetic field generates currents that hold constant the internal field within the conductor. Thus the IMF must take shape of a spiral like the solar wind particles [28].

Satellite measurements show alternating sectors of the field to be directed principally toward or away from the Sun. There are usually either two sectors, consistent with a coronal structure based on the assumption that the solar magnetic field is a dipole, or four sectors, consistent with a solar magnetic field imposed on the corona with a significant quadrupole component. Dynamic solar processes modify the solar-coronal dipole magnetic field into a unique pattern that opens the field lines at high latitudes and forms an equatorial heliospheric current sheet, separating currents directed toward and away from the Sun. The field polarity along the open field lines is

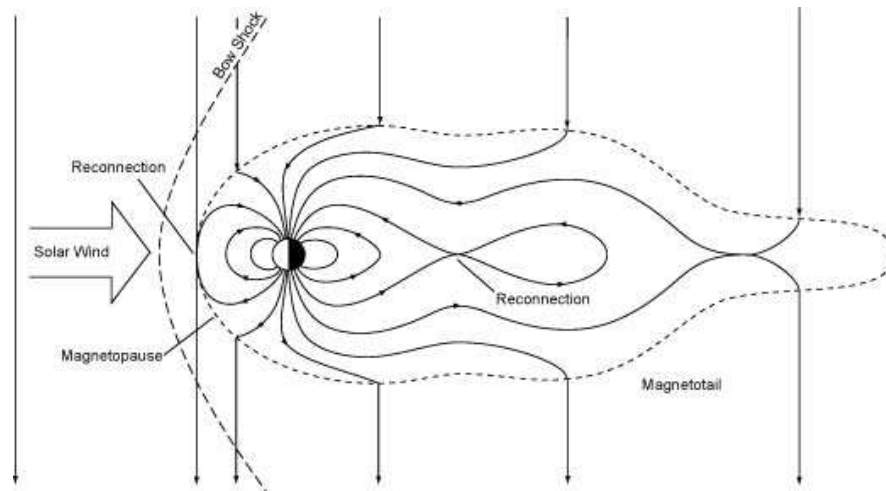


Figure 4.3: Model of the magnetosphere. The figure is downloaded from <http://geomag.usgs.gov/intro.php>.

identified with the polar region in which the field line originates. Active processes on the solar surface modify the systematic pattern of the equatorial current sheet into a “ballerina skirt” pattern such that the Earth’s environment is awash in the solar fields, sometimes directed from the solar north polar region and sometimes toward the south. These fields form the observed toward and away sectors. The sector fields keep its direction for about a week at a time and then changes in a relatively short time to the opposite polarity. This pattern has been found to repeat with a period of 27 days, which is the Sun’s rotation period viewed by an observer moving around the Sun with the Earth. Therefore this recurrency tendency suggests explanation in terms of sources fixed on the Sun and swept past the Earth by solar rotation. For a tilted-dipole corona, rotation of the interplanetary magnetic pattern would place a stationary observer alternately above and below the heliospheric current sheet, or alternately in two regions of opposite magnetic polarity, during each 27-day period. With a quadrupole solar magnetic field the polarity pattern has more frequent crossings of the neutral line and thus shorter intervals of unchanging polarity, but with the same basic 27-day period for repetition of the entire pattern [28], [29].

As the solar-wind particles and the IMF encounter the Earth’s magnetosphere, which is the region defined by the presence of the Earth’s main field in space, a shock is formed. The region of the magnetosphere just inside the envelope that contains the characteristic fields and particles is called the magnetopause. The magnetopause is usually positioned between 5 to 20 Earth radii,

while the bow shock, following a parabolic shape, is usually 3 to 4 Earth radii farther from the Earth, as shown in Figure 4.3.

4.3 The Auroral Electrojet Index

The Auroral Electrojet (AE) Index is one of several geomagnetic indices for providing a global picture of degree of disturbance level. The principal geomagnetic disturbance index is the K index obtained from the H -component of field, or the D -component if it is more disturbed than H (see Figure 4.4), and divides activity into ten levels. An estimated value of the local quiet daily variation is subtracted from the daily records and the range value of geomagnetic activity is determined for each 3-hour UT period at individual observatories. Using a predetermined adjustment to match the statistical occurrences of activity levels among the contributing stations, a 0-to-9 scale value is assigned to the disturbance level. K_p is a “planetary” indication of activity, and is derived using an average of 11 selected observatory K values [28].

The AE index is a measure of the aurora-related magnetic activity around the auroral oval of the Northern Hemisphere. The H -component field variations are measured at observatories along the auroral zone. The sampled data is then superposed and plotted together with the universal time (UT) on the x -axis and the value of the data on the y -axis. The upper envelope and the lower envelope of the plot are called the AU and AL respectively, and the AE index is the difference between these [28].

To get a better understanding of what the AE index represents, we must look into the features of a magnetic storm. The magnetospheric substorm is defined as a more or less predictable sequence of changes in the magnetosphere each time the interplanetary field turns southward [29]. When the IMF remains southward for an extended interval, auroral currents become continually disturbed. The geomagnetic field and the IMF reconnects, and there are open and closed field lines (See Figure 4.3, the open field lines are the Earth’s magnetic field lines connected to the IMF, the closed ones are the Earth’s magnetic field lines closed around Earth). Plasma will flow along the open field lines and into the magnetosphere. The injected particles drift in a ring around the Earth, protons drift westward and electrons drift eastward, creating a westward current in the distances 3-5 Earth radii called the ring current. Additional partial-ring currents also flow partway around the Earth in the middle of the magnetosphere. Birkeland currents connect the ends of the partial rings to the ionosphere, where conduction currents can complete the circuit. The region-1 Birkeland currents are near the poleward edge of the auroral zone, and go down into the ionosphere on the dawnside, and up from the ionosphere on the duskside. The region-2 Birkeland currents are in the more equatorward part of the auroral zone, and go up from the ionosphere on the dawnside, and down into the ionosphere on the duskside. The Birkeland

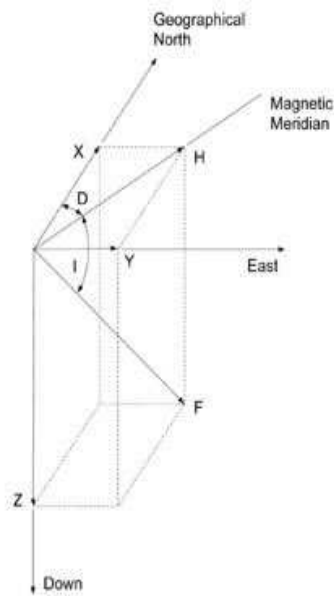


Figure 4.4: The geomagnetic field in different coordinate systems. F is the total field intensity. X , Y and Z are the cartesian components of the field with respect to a geographic coordinate system, where X is northward, Y is eastward and Z is vertically down toward the center of the Earth. H is the magnitude of the field projected in the horizontal plane, D is the declination angle measured positive from north to east and I is the inclination angle made by the the total-field vector with respect to the horizontal plane and is positive for vectors below the plane. The figure is downloaded from <http://geomag.usgs.gov/intro.php>.

currents give rise to the auroral electrojet, an intense westward ionospheric current in the auroral nightside ionosphere, flowing in the region of enhanced conductivity created along with the auroras. The electrojet current depresses the northward geomagnetic field at those latitudes with violent variations in synchronization with the overhead auroras. The conducting lower F-region and E-region ionosphere allows a closure of the strong substorm westward electrojets to be communicated to other longitude and lower-latitude ionospheric locations. Compared to the magnetospheric current systems, ionospheric currents are a short distance from the observatories at the surface, so these currents have a major influence upon the H , D , and Z variation fields. The Auroral Electrojet Indices, representing AU, AL, AE and AO (the mean of AU and AL), were defined by Davis and Sugiura [30] in 1966 for obtaining a measure of the strength of the auroral electrojets relatively uncontaminated by effects of the ring current.

A substorm is often divided into four phases; the quiet phase, the growth phase, the expansion phase and the recovery phase. The AE indices can describe the different phases of a substorm [29]. The beginning and the end of a substorm can be defined by the the departure and return of AU and AL to background levels defined by variations during a quiet day. The growth phase is the initial interval of slowly growing AU and AL. During the expansion phase several distinct intensifications of the AL index occur. Eventually the AL index reaches a minimum and begins to recover. AL increases, and the substorm is in its recovery phase. The current systems dies away, and the substorm ends. The rise and fall of the substorm electrojet constitute only the expansion and early recovery phase.

4.4 The Disturbance Storm Time Index

The disturbance storm time (D_{st}) index is an hourly index, and is a measure of the strength of the ring current mentioned in section 4.3. The index is calculated by a technique similar to that used in the AE index. Some refinements are necessary because secular variations and diurnal variations at each station can be as large as the storm time disturbance. The basic problem is to define a sequence of quiet values that can be used to define the trend and the seasonally dependent diurnal variation. Quiet days often occur in the recovery phase of magnetic storms, and at such times the H trace is depressed, but is increasing exponentially with time. If these days are included in the determination of the secular trend, the result will be biased to low values. A similar problem arises in obtaining an average quiet day appropriate to a season. Storm recovery tends to make the values of H at the ends of the days higher than at the beginnings. It is also hard to define a quiet day, as the most quiet day of a month not necessarily is very quiet. For the secular trend, the best that can be done is to take a sequence of midnight values that occur during rare instances of no activity, well separated from magnetic storm recoveries. A polynomial fit to these values can then be subtracted from all data acquired by a station in a given year. From these data, one then selects quiet intervals identified by for instance the AE index. These intervals are corrected for recovery trends, and offset to zero at local midnight to remove storm bias. The data are then arranged in a two-dimensional matrix with rows for each day and columns for each hour of the day, and a two-dimensional Fourier analysis is performed. Only the low harmonics are retained, and the trend coefficients and Fourier harmonics can be used to predict a quiet H at any time of day and year. When the quiet day is removed, the amplitude of the residual is adjusted by dividing by the cosine of the station's magnetic latitude. The modified residuals can then be plotted against a common baseline. The D_{st} index is defined as the instantaneous average around the world of the adjusted residuals [29].

4.5 Results

I have performed multifractal analysis on the IMF data and the AE index for quiet days and disturbed days to see if there are any differences in the spectra. The Kyoto database [26] provides a list with the dates for the most quiet and most disturbed days, where the selection of these is deduced from the K_p indices described in section 4.3. A relative order number is assigned to each day of the month, where this number is the average of three order numbers: the sum of the eight K_p values, the sum of squares of the eighth K_p values and the maximum of the eight K_p values. The days with the lowest and the highest mean order numbers are selected as the most quiet and most disturbed days respectively [31].

It should be noted that these selection criteria give only a relative indication of the character of the selected days with respect to the other days of the same month. As the general disturbance level may be quite different for different years and also for different months of the same year, the selected most quiet days of a month may sometimes be rather disturbed or vice versa. At [31] there are tables where the quiet days that are not really quiet and the disturbed days that are not really disturbed are marked. The tables at [26] does not contain this information, but unfortunately this was discovered too late, so I have not taken this into consideration when choosing data to analyse, using the tables at [26].

I picked data with 1-minute time resolution from the most disturbed day each month and made a time series with data from each month during a year, giving a time series with with 17280 points. I wanted to analyse data for each year during solar cycle 23, starting in 1996 and ending i 2006, with solar maximum in 1999. NASA's Coordinated Data Analysis Web [23] contained data for all of the years in question, but data for 1996 and 2006 were unfortunately misssing in the Kyoto database [26]. Therefore I could not analyse the AE index for the solar minima. I made time series for each year and analysed these separately. I then repeated the procedure for the quiet day data. At the boundary of the solar wind and magnetosphere, the solar-magnetospheric system is usually used, where X points to the Sun, Z points northward and dipole in the $X - Z$ plane. For the IMF data, I therefore performed the analysis on B_x , B_y and B_z in GSM coordinates for disturbed and quiet day data. Finally, I compared the generalized dimension spectra for solar minimum and solar maximum with the generalized dimension spectrum for the p-model

mentioned in section 3.2. This has the generalized dimension

$$D_q = \frac{1}{q-1} \frac{\log(p_1^q + p_2^q)}{\log 2}.$$

I also performed multifractal analysis on the D_{st} index. This is an hourly index, therefore I made time series with data for a whole year at a time, instead of distinguishing between quiet day data and disturbed data. I made time series for each year from 1996 to 2005. For 2006 the data were in a different format, therefore I did not perform analysis on data from this year. I then got time series with 8760 points (8784 for leap years, which occurred in 1996, 2000 and 2004). I compared the generalized dimension spectra with the p-model spectrum for these data as well.

I implemented the coarse analysis method in Mathematica. I used Eq. (2.31) to find the measure $\mu([t, \Delta t])$, and then Eq (2.32) to calculate the partition function. The partition function was then plotted versus the scale, Δt , for different qs . I used the scales $\Delta t = 2^n, n = 1, \dots, N - 1$, with 2^N equal to the total number of points in the time series. With time series with ~ 17000 points available for the IMF data and the AE index I therefore used the $2^{14} = 16384$ first points from the time series in the analysis. For some of the datafiles data were missing, and only $2^{13} = 8192$ points could be used. For the Dst index I used the 2^{13} first points of the time series. The objective with plotting the partition function was to find the slope where this function is a straight line, $\tau(q)$, and use this to find the generalized dimension, $D_q = \tau(q)/(q - 1)$. I then used Eq.(2.18) and Eq.(2.19) to obtain the f - α curve. The Mathematica notebook used to implement the analysis is to be found in Appendix A-1.

Figure 4.5 and Figure 4.6 shows the spectra for the B_x -component of the IMF in 1999 (solar maximum) and 2006 (solar minimum) respectively. All spectra for the whole solar cycle can be found in Appendix B-1. The spectra shows the shapes of typical multifractal spectra (Figure 2.1). The B_x -component of the interplanetary magnetic field at the Earth's bow shock nose is clearly multifractal. The spectrum for the quiet day data in 1999 shown in Figure 4.5(a) has a very good fit with the p-model spectrum with $p_1 = 0.62$. The spectrum for the disturbed day data in 1999 shown in Figure 4.5(c) has a quite good fit with the p-model spectrum with $p_1 = 0.64$. For 2006, the quiet day spectrum in Figure 4.6(a) has a quite good fit with the spectrum for the p-model with $p_1 = 0.64$, while for the disturbed day data in Figure 4.6(c) the spectrum has a fit with $p_1 = 0.62$. The figures show little differences in the spectra for quiet days and disturbed days. The f - α curve is somewhat broader for disturbed day data than for quiet day data around

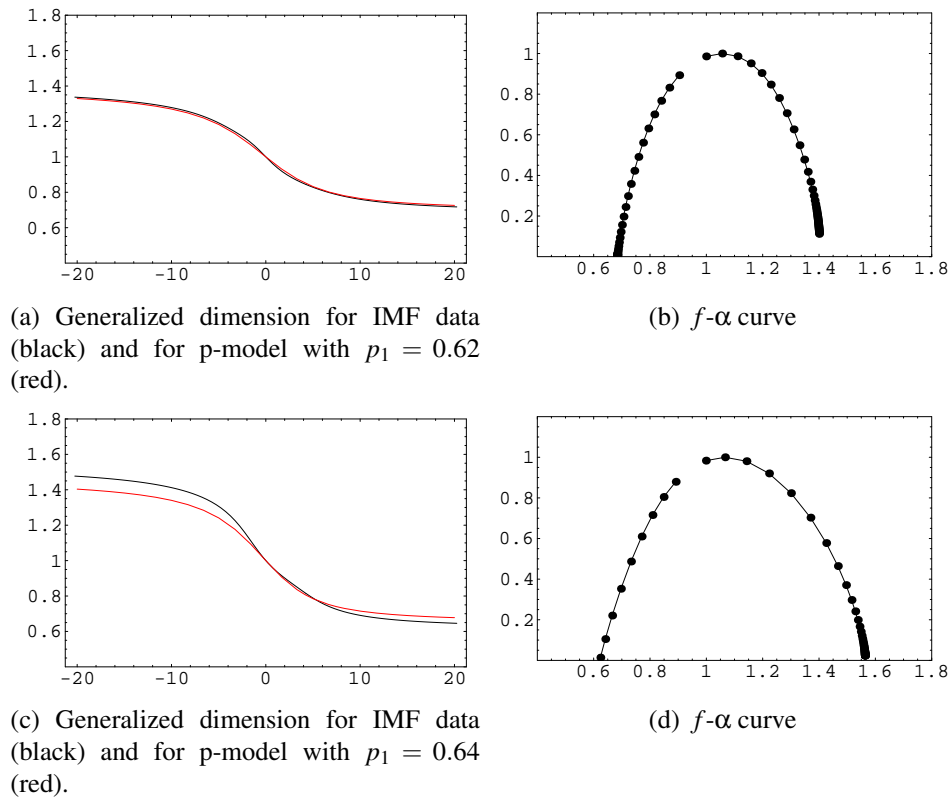
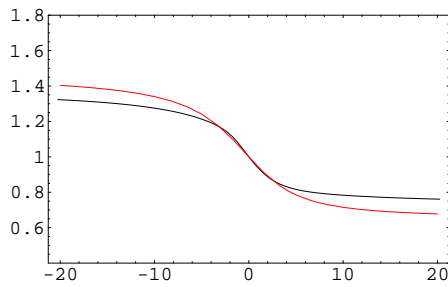
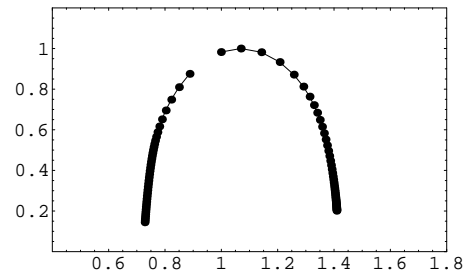


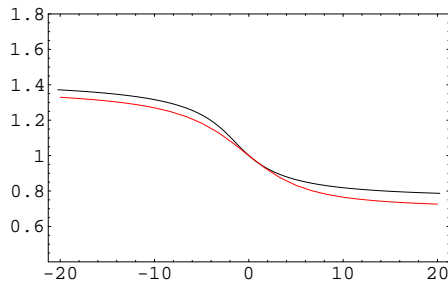
Figure 4.5: Spectra for quiet day data ((a) and (b)) and disturbed day data ((c) and (d)), for the IMF B_x -component, 1999.



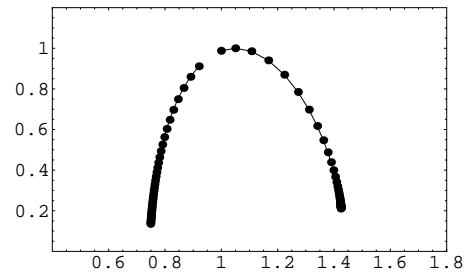
(a) Generalized dimension for IMF data (black) and for p-model with $p_1 = 0.64$ (red).



(b) f - α curve



(c) Generalized dimension for IMF data (black) and for p-model with $p_1 = 0.62$ (red).



(d) f - α curve

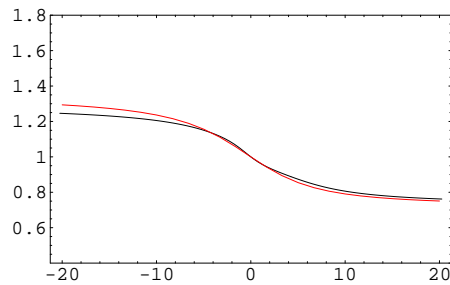
Figure 4.6: Spectra for quiet day data ((a) and (b)) and disturbed day data ((c) and (d)), for the IMF B_x -component, 2006.

solar maximum, but keep very similar for the rest of the solar cycle. For the most narrow singularity spectra, $f(\alpha)$ is positive for $0.8 < \alpha < 1.4$, and for the broadest $f(\alpha)$ for $0.6 < \alpha < 1.6$.

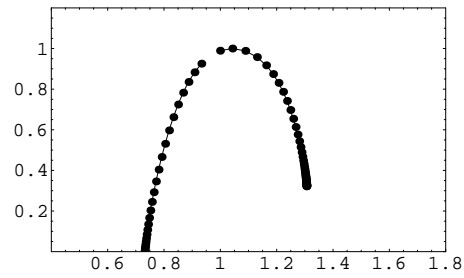
Figure 4.7 and Figure 4.8 shows the spectra for the B_y -component of the IMF in 1999 (solar maximum) and 2006 (solar minimum) respectively. All spectra for the whole solar cycle can be found in Appendix B-2. The spectra shows the shapes of typical multifractal spectra (Figure 2.1). The B_y -component of the interplanetary magnetic field at the Earth's bow shock nose is clearly multifractal. For 1999, the spectrum for the quiet day data in Figure 4.7(a) has a good fit with the p-model spectrum with $p_1 = 0.61$. The spectrum for the disturbed day data in Figure 4.7(c) has a good fit with the spectrum for the p-model with $p_1 = 0.63$. For both quiet and disturbed day data the fit is best for $q > 0$. The spectrum for quiet day data in 2006 in Figure 4.8(a) has a fit with the p-model specter with $p_1 = 0.63$, and the spectrum for disturbed day data in Figure 4.8(c) has a somewhat better fit with the p-model spectrum with $p_1 = 0.64$. The figures show little differences in the spectra for quiet days and disturbed days. The f - α curve is somewhat broader for disturbed day data than for quiet day data around solar maximum, but keep very similar for the rest of the solar cycle. For the most narrow singularity spectra, $f(\alpha)$ is positive for $0.8 < \alpha < 1.4$, and for the broadest $f(\alpha)$ for $0.55 < \alpha < 1.6$.

Figure 4.9 and Figure 4.10 shows the spectra for the B_z -component of the IMF in 1999 (solar maximum) and 2006 (solar minimum) respectively. All spectra for the whole solar cycle can be found in Appendix B-3. The spectra shows the shapes of typical multifractal spectra (Figure 2.1). The B_z -component of the interplanetary magnetic field at the Earth's bow shock nose is clearly multifractal. The quiet day data spectrum for 1999 in Figure 4.9(a) has a quite good fit with the p-model spectrum with $p_1 = 0.6$, while the disturbed day data spectrum in Figure 4.9(c) has a very good fit with the p-model with $p_1 = 0.63$ for $q > 0$, but a discrepancy between the spectra shows for $q > 0$. For the spectrum for quiet day data in 2006 in Figure 4.10(a) there is a very good fit with the p-model with $p_1 = 0.65$, but there is a small discrepancy for $q < 0$. For the disturbed day data spectrum, a quite good fit with the p-model with $p_1 = 0.64$ is found. The figures show little differences in the spectra for quiet days and disturbed days. The f - α curve is somewhat broader for disturbed day data than for quiet day data around solar maximum. For the rest of the cycle there are no great differences in the spectra. For the most narrow singularity spectra, $f(\alpha)$ is positive for $0.8 < \alpha < 1.4$, and for the broadest $f(\alpha)$ for $0.55 < \alpha < 1.6$.

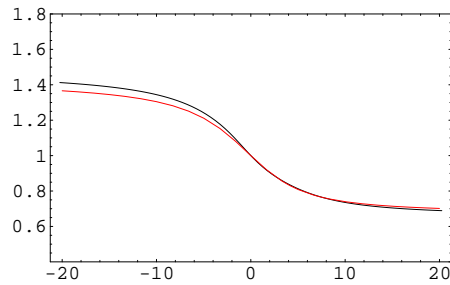
Figure 4.11 shows the spectra for 1999 (solar maximum) and Figure 4.12 shows the spectra



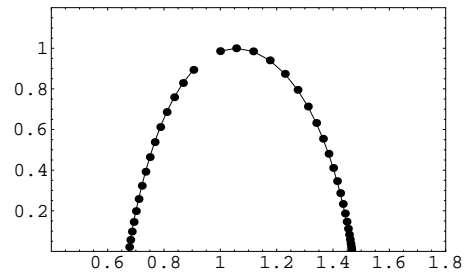
(a) Generalized dimension for IMF data (black) and for p-model with $p_1 = 0.61$ (red).



(b) f - α curve

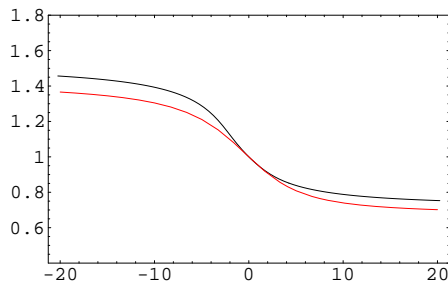


(c) Generalized dimension for IMF data (black) and for p-model with $p_1 = 0.63$ (red).

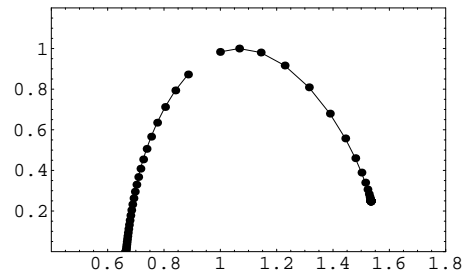


(d) f - α curve

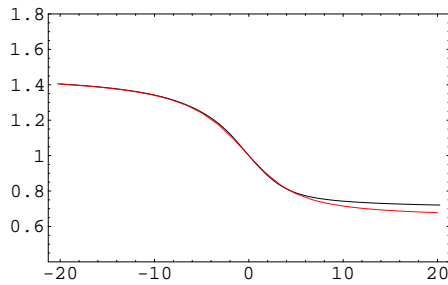
Figure 4.7: Spectra for quiet day data ((a) and (b)) and disturbed day data ((c) and (d)), for the IMF B_y -component, 1999.



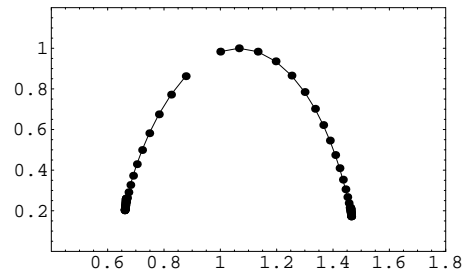
(a) Generalized dimension for IMF data (black) and for p-model with $p_1 = 0.63$ (red).



(b) f - α curve

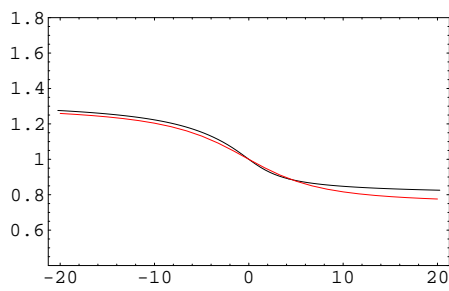


(c) Generalized dimension for IMF data (black) and for p-model with $p_1 = 0.64$ (red).

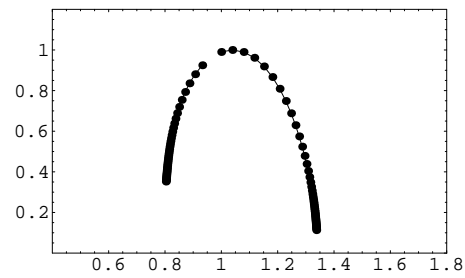


(d) f - α curve

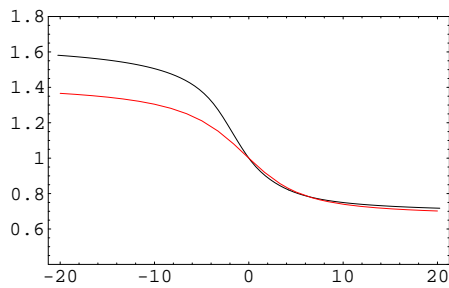
Figure 4.8: Spectra for quiet day data ((a) and (b)) and disturbed day data ((c) and (d)), for the IMF B_y -component, 2006.



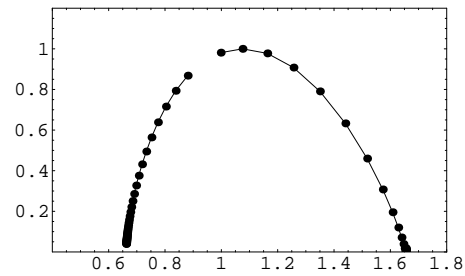
(a) Generalized dimension for IMF data (black) and for p-model with $p_1 = 0.6$ (red).



(b) f - α curve

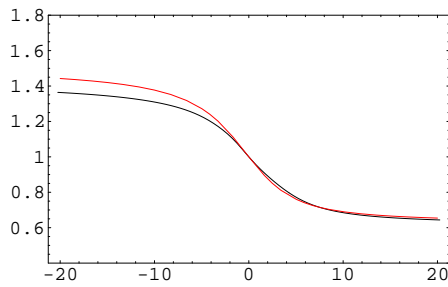


(c) Generalized dimension for IMF data (black) and for p-model with $p_1 = 0.63$ (red).

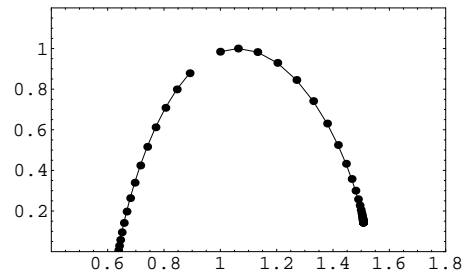


(d) f - α curve

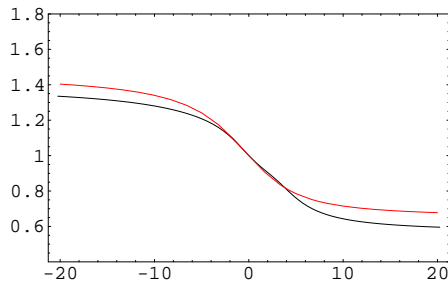
Figure 4.9: Spectra for quiet day data ((a) and (b)) and disturbed day data ((c) and (d)), for the IMF B_z -component, 1999.



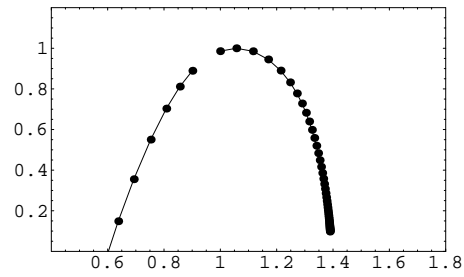
(a) Generalized dimension for IMF data (black) and for p-model with $p_1 = 0.65$ (red).



(b) f - α curve



(c) Generalized dimension for IMF data (black) and for p-model with $p_1 = 0.64$ (red).



(d) f - α curve

Figure 4.10: Spectra for quiet day data ((a) and (b)) and disturbed day data ((c) and (d)), for the IMF B_z -component2006.

for 2005 (the year before solar minimum occurred) for the AE index. The spectra for all the years from 1997 to 2005 can be found in Appendix B-4. The spectra has the typical shapes of multifractal spectra in Figure 2.1. The AE index does clearly have multifractal properties. For 1999, the quiet day data spectrum in Figure 4.11(a) has a very good fit with the spectrum for the p-model with $p_1 = 0.66$ for $q > 0$, while the disturbed day data spectrum in Figure 4.11(c) has an overall good fit with the spectrum for the p-model with the same parameter. For 2005 both the quiet day data spectrum and the disturbed day data spectrum in Figure 4.12(a) and Figure 4.12(c) respectively has a very good fit with the p-model spectrum with $p_1 = 0.65$. Comparing the spectra for quiet day data and disturbed day data, there are little variations. The spectra also keep very similar during the solar cycle. For the most narrow singularity spectra, $f(\alpha)$ is positive for $0.6 < \alpha < 1.4$, and for the broadest $f(\alpha)$ for $0.6 < \alpha < 1.75$.

Figure 4.13 shows the spectra for 1996 (solar minimum) and Figure 4.14 shows the spectra for 1999 (solar maximum) for the D_{st} index. The spectra for all the years from 1996 to 2005 can be found in Appendix B-5. The spectra does not have the typical shapes of multifractal spectra in Figure 2.1. Comparing with the spectra for the sandpile model, some of the spectra look almost monofractal. Other spectra do not look exactly monofractal, but their f - α curve is not as symmetric as for the typical multifractal spectra. Some f - α curves also shows a small cluster of points around the box dimension, and not the typical distribution of dimensions with few points around the box dimension, and more and more points as $|q| \rightarrow \infty$. Still, the generalized dimension spectrum for 1996 has a very good fit with the p-model spectrum with $p_1 = 0.58$, and the spectrum for 1999 has a quite good fit with the spectrum for the p-model with $p_1 = 0.63$. There are differences in the spectra during the solar cycle, but it is hard to say if this is due to variations in sunspot activity. For the most narrow singularity spectra, $f(\alpha)$ is positive for $0.75 < \alpha < 1.1$, and for the broadest $f(\alpha)$ for $0.6 < \alpha < 1.3$.

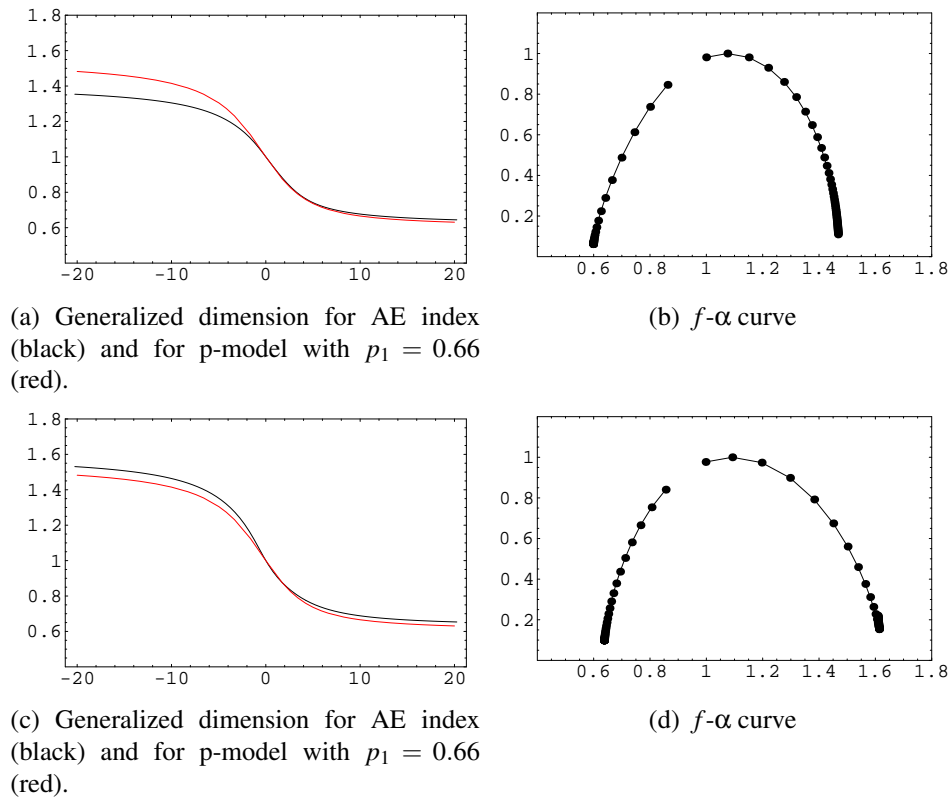
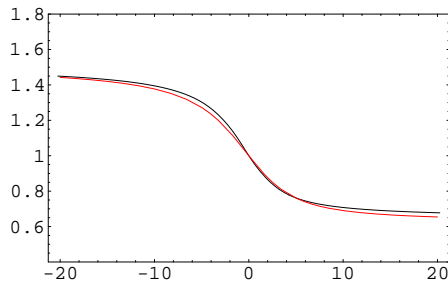
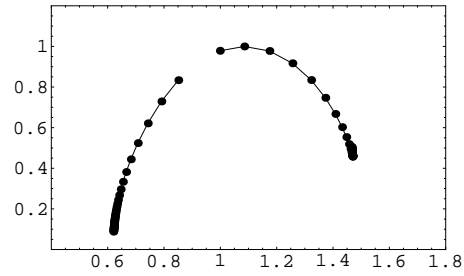


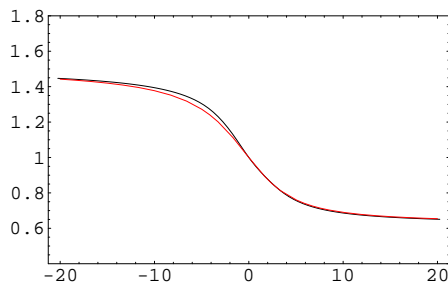
Figure 4.11: Spectra for quiet day data ((a) and (b)) and disturbed day data ((c) and (d)), for the AE index, 1999.



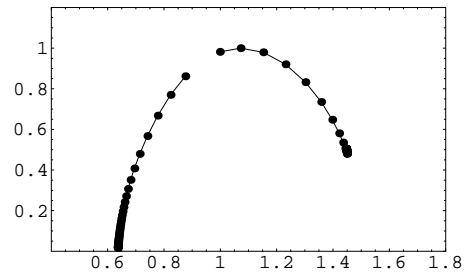
(a) Generalized dimension for AE index (black) and for p-model with $p_1 = 0.65$ (red).



(b) f - α curve

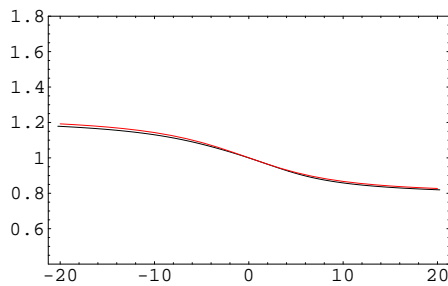


(c) Generalized dimension for AE index (black) and for p-model with $p_1 = 0.65$ (red).

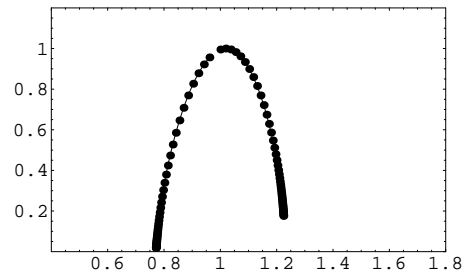


(d) f - α curve

Figure 4.12: Spectra for quiet day data ((a) and (b)) and disturbed day data ((c) and (d)), for the AE index, 2005.

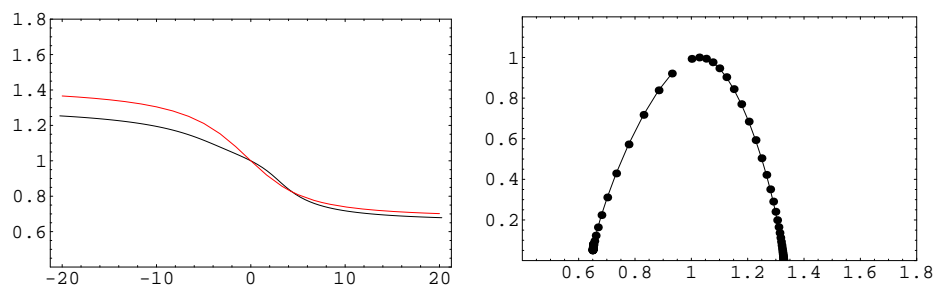


(a) Generalized dimension for D_{st} index (black) and for p-model with $p_1 = 0.58$ (red).



(b) f - α curve

Figure 4.13: Spectra for the D_{st} index, 1996.



(a) Generalized dimension for D_{st} index (black) and for p-model with $p_1 = 0.63$ (red).

(b) f - α curve

Figure 4.14: Spectra for the D_{st} index, 1999.

4.6 Discussion

Comparing the spectra for the IMF field strength with the spectra for the BTW sandpile model, the IMF is clearly multifractal. For all the components, B_x, B_y and B_z , the spectra kept very similar for quiet days and disturbed days during the solar cycle, except around solar maximum. Here the f - α curve was broader for disturbed day data than for quiet day data. As mentioned in section 4.5 I have not taken into account the differences in disturbance level for different periods. It might be that some of the days assumed to be disturbed were not really disturbed due to little activity that month, and also that some of the days assumed to be quiet were not really quiet due to high activity all through the month in question. Therefore it is hard to give any certain conclusions. One guess is that high activity level yield broader singularity spectra for the magnetic field strength than low activity level. If the differences between the activity level for quiet days and the activity level for disturbed days are greater during solar maximum than during solar minimum, there would be larger differences in the spectra around solar maximum. However, more than one solar cycle must be analysed to find out whether the solar cycle has an impact on width of the multifractal spectra or not. It must also be mentioned that for some of the IMF data files, quite a lot of data were missing. Missing data had been given the value 9999, and for the different years, I found between 500 and 3500 such values in my time series. I removed these points from the time series, so they do not directly alter the spectra, but it might be that the spectra had turned out differently if no data were missing in the downloaded datafiles. The method used for analysing the data is not perfectly accurate, and maybe for the time series where a lot of data were missing, errors in the spectra were larger. The analysis method is inaccurate for $q \ll 0$ especially, often yielding a broader spectrum than it should. This also makes it harder to give conclusions about how the sunspot cycle affects the spectra. The only thing one can conclude for certain is that the IMF strength is multifractal during all of the solar cycle for both disturbed and quiet days. This suggests that the IMF will not become monofractal or not fractal at all due to sunspot activity. The generalized dimension spectra had quite good fits with the p-model spectrum for $0.6 < p_1 < 0.65$. For the spectra where there were a discrepancy between the data spectrum and the p-model spectrum, I think the difference were due to errors in the data spectrum, rather than that the spectrum could not be compared to the p-model spectrum. The multifractal properties of the IMF data and the good fit with the p-model indicate that the IMF data are intermittent, and therefore turbulent.

The AE index spectra also show a multifractal nature. There are small differences in the spectra during the solar cycle, but not clearly due to sunspot activity. There are no great differences in

the spectra for quiet and disturbed days, so it seems that the activity level has little impact on the AE index. As for the IMF data, the analysis method may give errors in the spectra, but when analysing the AE index, I found that multifractality were more clearly shown, as the plotting of the partition function as a function of scale displayed straighter lines than for the IMF data. Data were missing for July 1997 and November 1998, so for these years I had to use shorter time series in the analysis than for the rest of the solar cycle. Except from that, there were no missing data, so this was not a problem in the same way as it was for the IMF data. The generalized dimension spectra could be very well fitted with the p-model spectrum for $p_1 = 0.65$ and $p_1 = 0.66$. The multifractal properties of the AE index and the good fit with the p-model spectrum indicate that the AE index is intermittent and turbulent. Consolini et al. [32] have found similar results. Other kinds of analysis that indicate intermittence have been performed [34], which adds proof that the AE index indeed is turbulent.

The D_{st} index does not show multifractal properties as clearly as the other data. The singularity spectra are more narrow, and comparing them to the BTW sandpile model spectra, the spectra could be interpreted as monofractal spectra for some of the years. Spectra for other years look more multifractal, but do not have $f-\alpha$ curves that are as symmetric as the typical ones for multifractals. There is also a cluster of points around the box dimension in some of the $f-\alpha$ curves that are not typical for perfect multifractals. Balasis [33] suggests that the D_{st} index has an intermittent nature, and in that case it must be multifractal. However, [33] focus mainly on the D_{st} index for 2001. Maybe the D_{st} index is multifractal under some conditions, and monofractal under other. The generalized dimension spectrum for 1996 has a very good fit with the p-model spectrum with $p_1 = 0.58$, and the spectrum for 1999 has a quite good fit with the spectrum for the p-model with $p_1 = 0.63$. For a monofractal, $p_1 = 0.5$. Whether the low value of p_1 for 1996 should be interpreted as no intermittence or weak intermittence is not for me to say. With a more accurate analysis method this might be clearer. It seems like the D_{st} is multifractal, and thus intermittent, at least under some conditions, but maybe not for all. Just from looking at the spectra for 1996 and 1999 I am tempted to say that the D_{st} index shows stronger multifractality around solar maximum than when solar minimum occurs. Looking at the rest of the spectra (Appendix B-5), I am not so sure about that, and maybe other dynamics play a stronger part. Again, it is hard to say with only one solar cycle analysed. No data were missing in the datafile downloaded, so I cannot use that as an excuse for finding it hard to interpret the spectra. However, the D_{st} index has a 1-hour time resolution, while the other data have a 1-minute time resolution. It might be that intermittence is present mostly for short time scales.

Analysing these time series, 2^{13} or 2^{14} points were used. When analysing generated time series, 2^{18} points were used and only the largest scales considered when finding the spectra. With longer time series available maybe more accurate results could have been obtained for the real data as well. However, fractals occurring in nature are only multifractal for a given range of scales, and using just the largest scales when analysing might yield different results. With a better time resolution for the real data, the same scales could be considered, but more points used, maybe yielding more accurate results. It might then be clearer whether the D_{st} index is multifractal or monofractal, and for what conditions fractality occur.

Chapter 5

Conclusions

The analysis method used in this thesis give good enough results for data that clearly are multifractal, but yield too inaccurate results for deciding whether monofractality or multifractality occurs in some cases. However, with better time resolution and more points available, the method could yield more accurate results. The WTMM method might yield a somewhat better accuracy, but according to Oświęcimka [11], large errors for $q \ll 0$ occur applying this method as well. The MFDFA method is found to give very good accuracy in the singularity spectrum for Brownian motion and fractional Brownian motion in [11]. For future work it would be interesting to study these methods for analysing time series from naturally occurring fractals, and compare the spectra resulting from the different analysis methods. For time independent data series the use of the generalized correlation sum in Eq. (2.11) in multifractal analysis is often preferred to using the moment function in Eq. (2.5), since the last method requires large computer memory to get satisfactory accuracy, which makes the computation slow [7]. Still, the use of the generalized correlation sum gives inaccurate results for $q \ll 0$, and maybe the detrended fluctuation analysis is better for both time series and series that are time independent.

Fractals are found in a wide range of fields, and more and more phenomena within the variety of fields are found to be fractal. The fractal properties give information about the different phenomena, for instance if turbulence occurs. Knowledge about different phenomena is interesting in itself, and for instance in medicine multifractal analysis can be quite important, as the analysis can add diagnostic power if a patient has congestive heart failure. Nature seems to organize itself into different kinds of fractals in both space and time in numerous cases. Fractal analysis is important to get knowledge about many phenomena in natural sciences, and applications to health science and social science are also found.

The analysis performed in this thesis confirm that the interplanetary magnetic field strength and the AE index have multifractal properties. Most of the f - α curves had positive $f(\alpha)$ for $0.6 < \alpha < 1.4$, but small variations occurred. All the spectra could be fitted well with the spectrum for the p-model for turbulence, which indicates that intermittence and turbulence is dominating in these dynamics. The analysis suggests that the D_{st} index is multifractal and intermittent under some conditions, but the singularity spectra are not as broad as for the IMF data and the AE index. Under some conditions, the D_{st} index seems to be very weakly intermittent or not intermittent at all.

Appendices

Appendix A-1: Mathematica Code

This appendix contains the code implemented in Mathematica notebooks used to perform multi-fractal analysis on different kinds of data.

```
SetDirectory["/Users/martin/Desktop/datadownloads/bxdist"];
```

```
<< Statistics`DataManipulation`
<< Graphics`Graphics`
```

Reading the file containing the data to be analysed.

```
bximf = ReadList["bxgsedist.dat", Number];

Length[bximf]

190080

yearlength = 12 * 24 * 60;
```

Data for all the years are contained in one file, so I take out data for the specific year I want to analyse for.

```
bx = Take[bximf, yearlength];
```

For missing data, the value 9999 is used. I want to delete these values, so I go through the data, find the index of these data and delete them.

```
missingdata = {};
For[i = 1, i ≤ Length[bx], If[bx[[i]] ≥ 9999, AppendTo[missingdata, {i}]; i++];

bx = Delete[bx, missingdata];

Length[bx]

14767

Npt = 2^13;
```

Differentiating the time series:

```
diff[v_] := Rest[v] - Drop[v, -1];
ydif = Take[diff[bx], Npt];
```

Finding the measure, μ .

```
mu[t_, q_] := (a = {}; boxsize = 2^t;
  For[i = 1, i ≤ Npt / (2^t), b = Sum[Abs[ydif[[j]]], {j, (i - 1) * boxsize + 1, i * boxsize}];
  If[b ≠ 0, a = Append[a, b]; i++]; Return[a^q])
```

Finding the moment function, M_q .

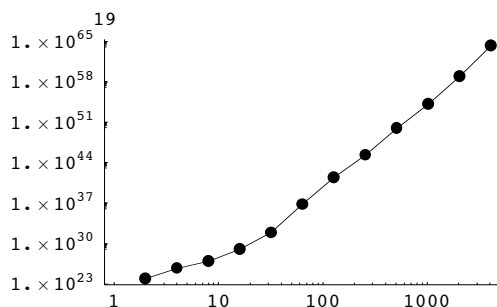
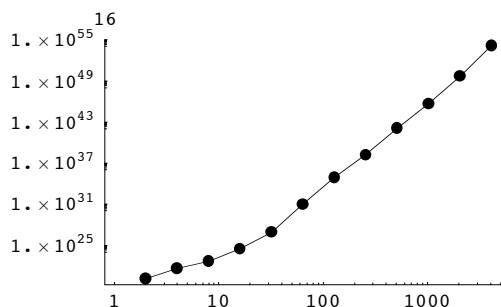
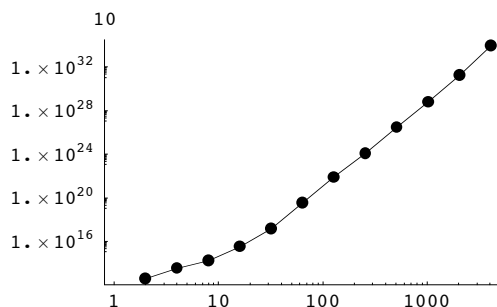
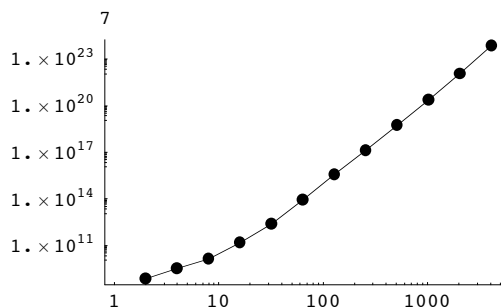
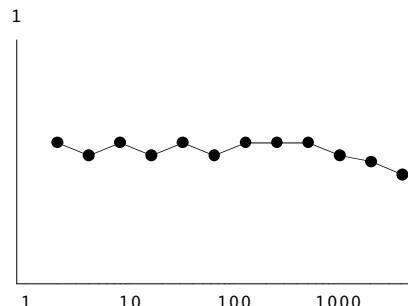
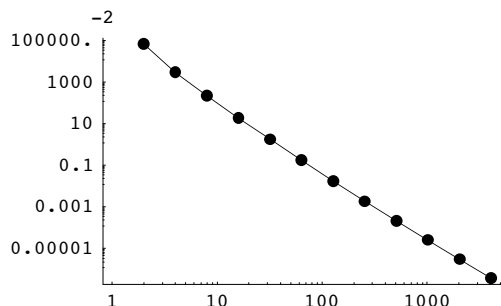
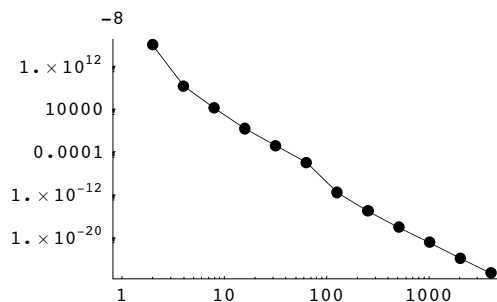
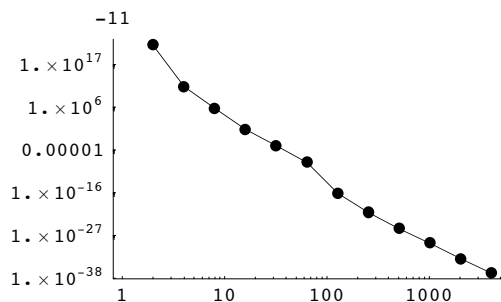
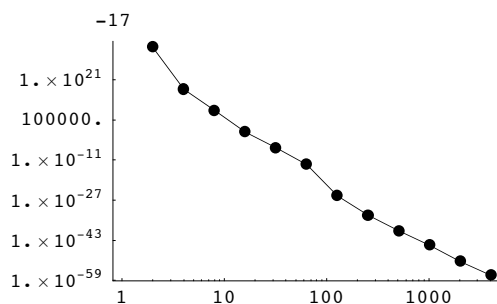
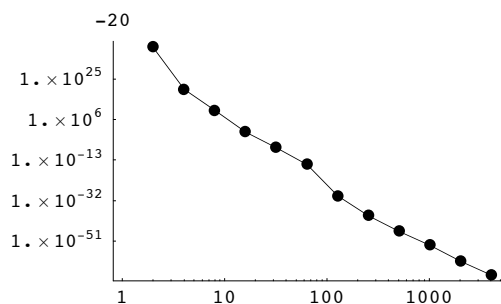
```
Mq[t_, q_] := Plus @@ mu[t, q];

mqtab[q_] = Table[{2^t, Mq[t, q]}, {t, 1, 12}];
```

Plotting the moment function as a function of scale.

```
structure = {};
For[q = -20, q ≤ 20, b = LogLogListPlot[mqtab[q],
  PlotStyle → PointSize[0.03], AxesLabel → q, DisplayFunction → Identity];
  c = LogLogListPlot[mqtab[q], AxesLabel → q, PlotJoined → True,
  DisplayFunction → Identity]; structure = Append[structure, Show[{b, c}]]; q = q + 3];
```

```
Show[GraphicsArray[{{structure[[1]], structure[[2]], structure[[3]]},  
  {structure[[4]], structure[[5]], structure[[6]]},  
  {structure[[7]], structure[[8]], structure[[9]]},  
  {structure[[10]], structure[[11]], structure[[12]]},  
  {structure[[13]], structure[[14]]}}, DisplayFunction -> $DisplayFunction]
```



Ticks::ticks : LogScale is not a valid tick specification. More...

- GraphicsArray -

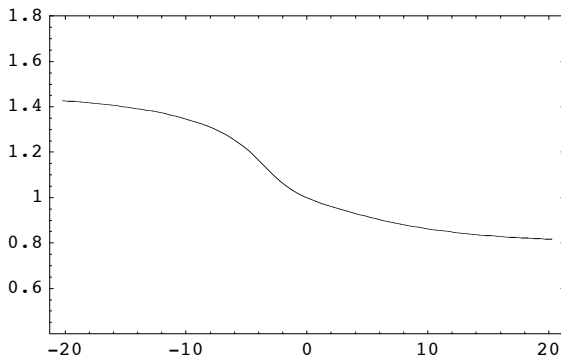
I find the slope of the structure function in the area where this is a straight line, and use this to find the generalized dimension, D_q .

```

Dq = {};
For[q = -20.25, q <= 20.25, d = LogLogListPlot[mqtab[q], DisplayFunction -> Identity];
  lp = Table[d[[1, j, 1]], {j, 5, 11}]; e = Simplify[Fit[lp, {x, 1}, x][[2]] / x];
  Dq = Append[Dq, {q, e / (q - 1)}]; q = q + 0.5];

dqplot =
  ListPlot[Dq, Axes -> False, Frame -> True, PlotRange -> {0.4, 1.8}, PlotJoined -> True]

```



- Graphics -

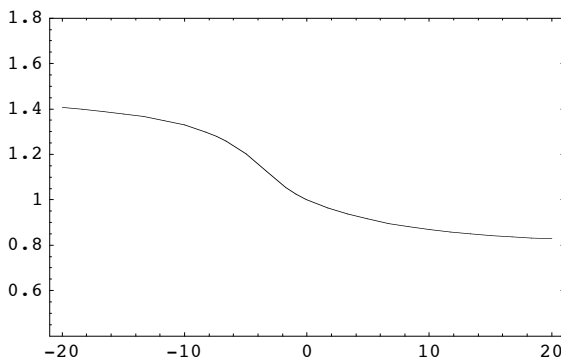
I find D_q as a continuous function of q , and then use this to find α and $f(\alpha)$.

```

Dqcont[q_] := Log[Mq[11, q] / Mq[5, q]] / ((q - 1) * Log[2^11 / 2^5]);

Plot[Dqcont[q], {q, -20, 20}, Axes -> False, Frame -> True, PlotRange -> {0.4, 1.8}]

```



- Graphics -

```

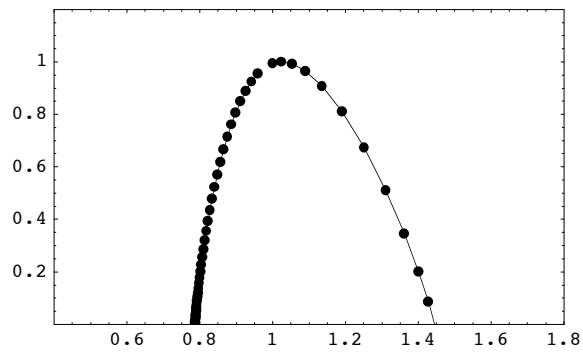
alpha[q_] := D[(r - 1) * Dqcont[r], r] /. r -> q;

f[q_] := q * alpha[q] - (q - 1) Dqcont[q];

fatab = Table[{alpha[q], f[q]}, {q, -20, 20, 0.5}];

```

```
points = ListPlot[fatab, Axes → False, Frame → True, PlotRange → {{0.4, 1.8}, {0, 1.2}},  
  PlotStyle → PointSize[0.02], DisplayFunction → Identity];  
curve = ListPlot[fatab, Axes → False, Frame → True, PlotRange → {{0.4, 1.8}, {0, 1.2}},  
  PlotJoined → True, DisplayFunction → Identity];  
Show[{points, curve}, DisplayFunction → $DisplayFunction]
```



- Graphics -

Appendix A-2: Generation of the BTW sandpile model activity signal

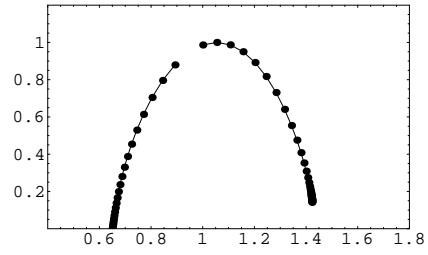
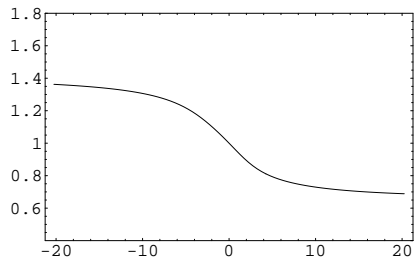
This appendix contains the code implemented in Mathematic for generation of the Bak-Tang-Wiesenfeld sandpile model activity signal.

```
n = 64;
X = Table[0, {n^2}];
a = 3; b = 3;
activity = {};

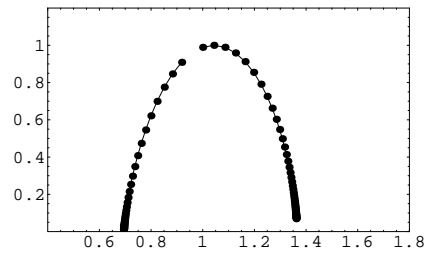
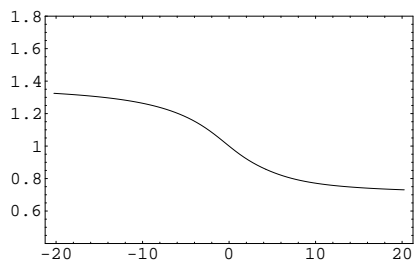
Do[
  While[X[[ (a - 1) * n + b]] < 4,
    a = Random[Integer, {2, n - 1}];
    b = Random[Integer, {2, n - 1}];
    X[[ (a - 1) * n + b]]++;
    activity = Append[activity, 0];
  ];
  oc = { (a - 1) * n + b};
  While[oc ≠ {},
    activity = Append[activity, Length[oc]];
    X[[oc]] = X[[oc]] - 4;
    Y = Partition[Join[oc + 1, oc - 1, oc + n, oc - n], 1];
    X = MapAt[# + 1 &, X, Y];
    X[[Range[n]]] = 0;
    X[[n * Range[n]]] = 0;
    X[[ (n^2 - n) + Range[n]]] = 0;
    X[[n * Range[0, n - 1] + 1]] = 0;
    oc = Union[Flatten[Y][[Flatten[Position[X[[Flatten[Y]]], _? (# > 3 &)]]]];
  ];
, {1000}]
```

Appendix B-1: Spectra for the IMF B_x -component

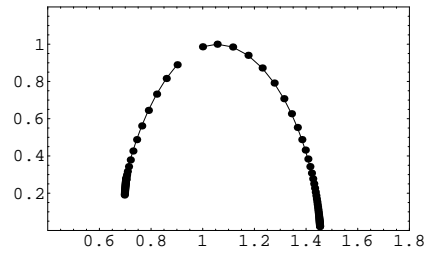
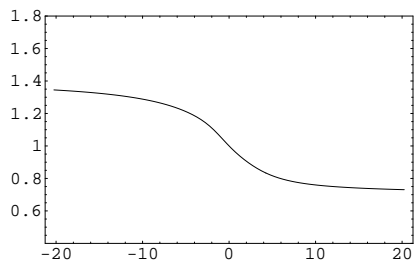
This appendix contains all the figures showing the generalized dimensions (left figures) and f - α curves (right figures) for the B_x -component of the interplanetary magnetic field for both quiet and disturbed days from 1996 to 2006.



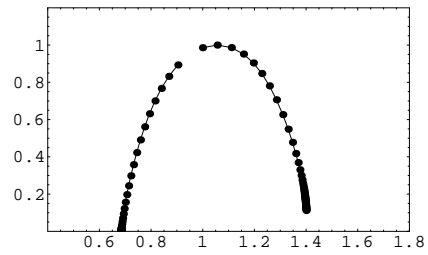
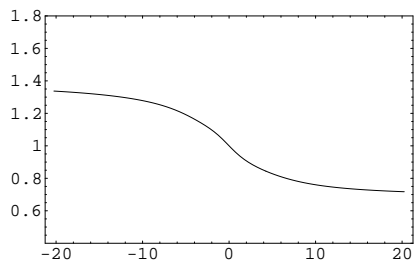
Quiet day data, 1996



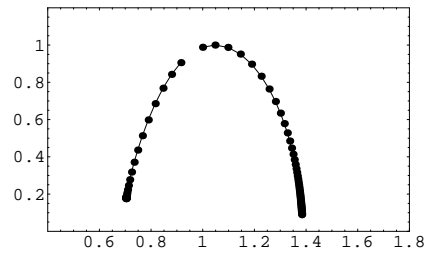
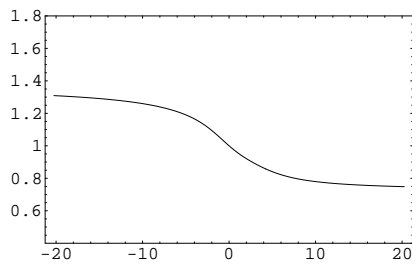
Quiet day data, 1997



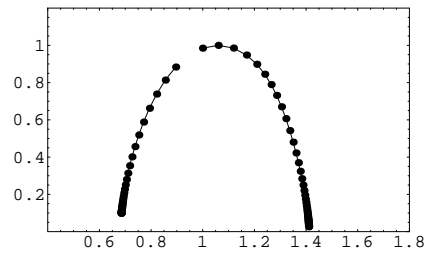
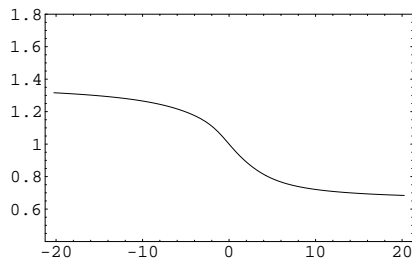
Quiet day data, 1998



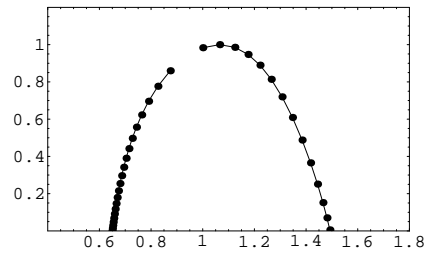
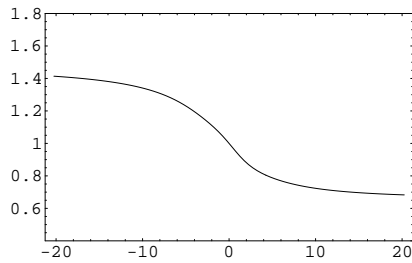
Quiet day data, 1999



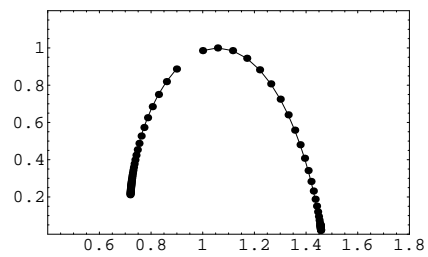
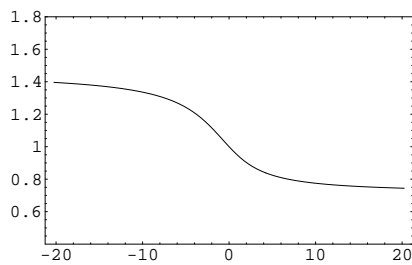
Quiet day data, 2000



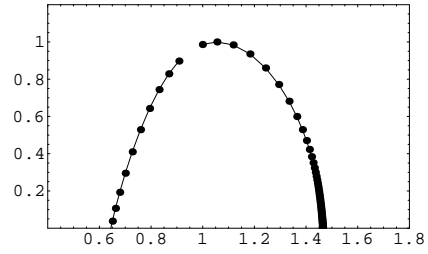
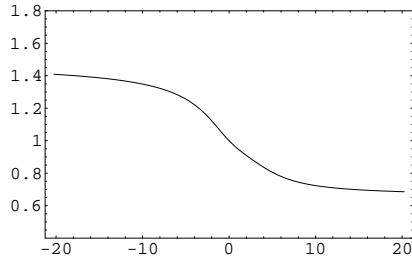
Quiet day data, 2001



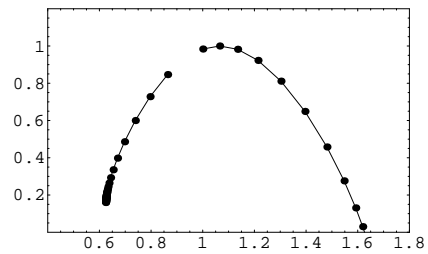
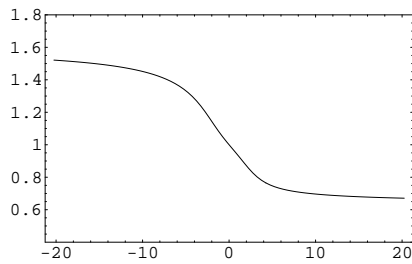
Quiet day data, 2002



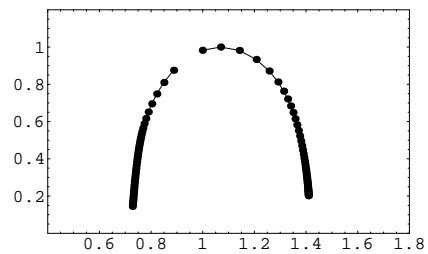
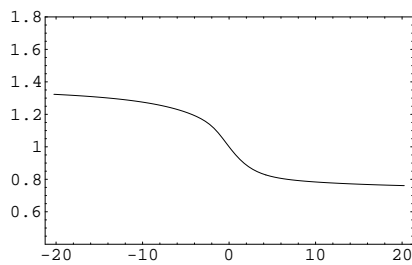
Quiet day data, 2003



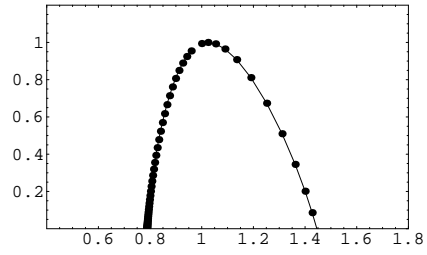
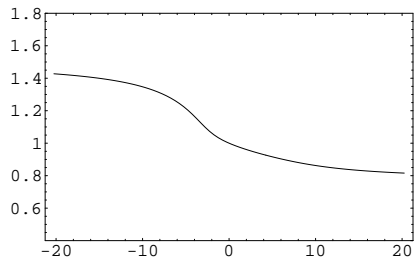
Quiet day data, 2004



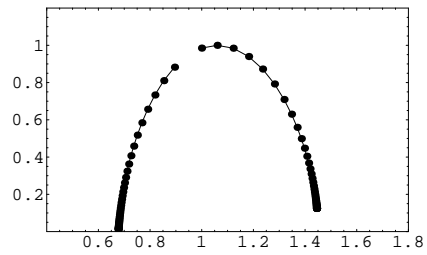
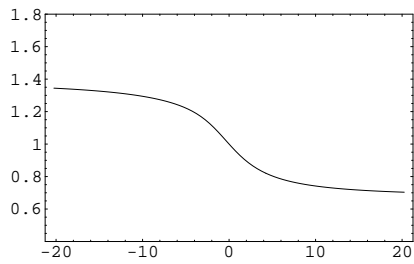
Quiet day data, 2005



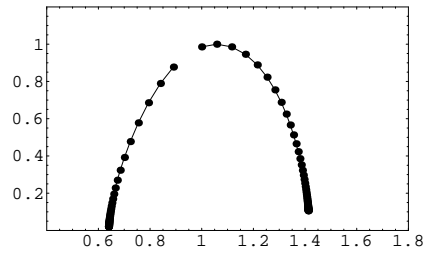
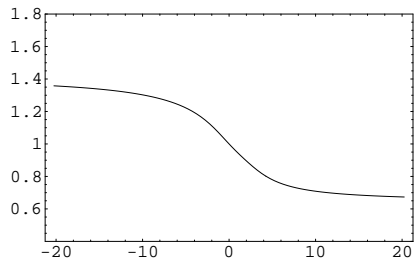
Quiet day data, 2006



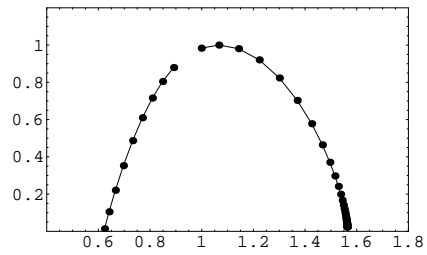
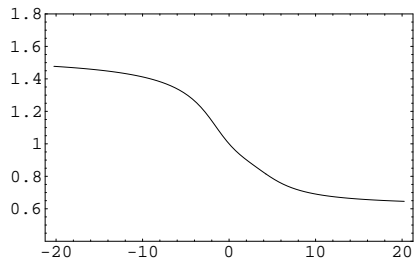
Disturbed day data, 1996



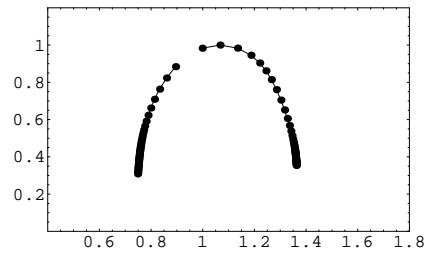
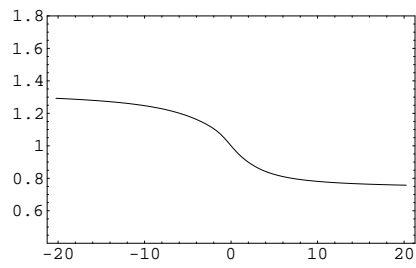
Disturbed day data, 1997



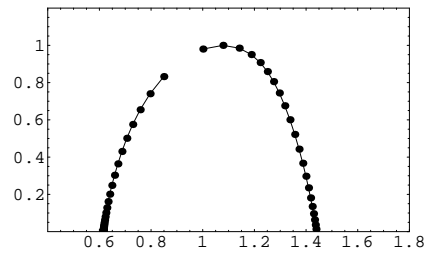
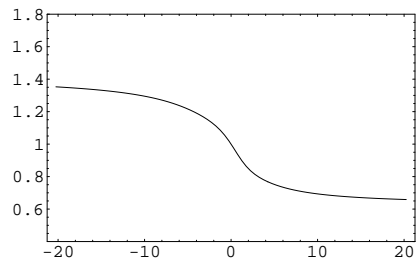
Disturbed day data, 1998



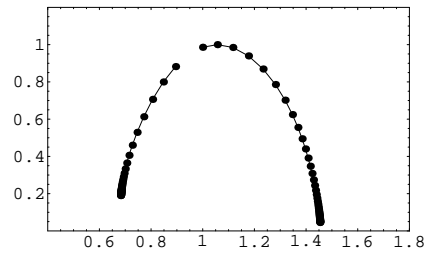
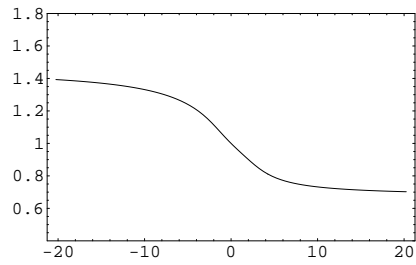
Disturbed day data, 1999



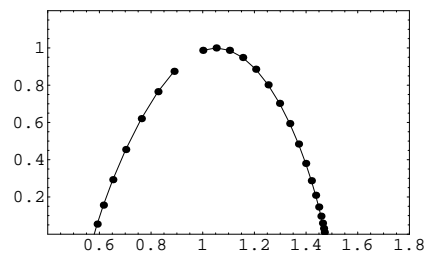
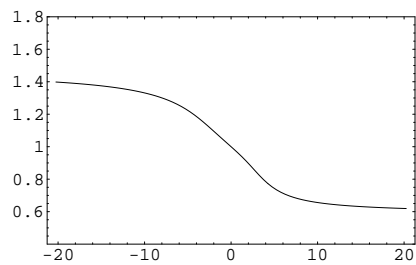
Disturbed day data, 2000



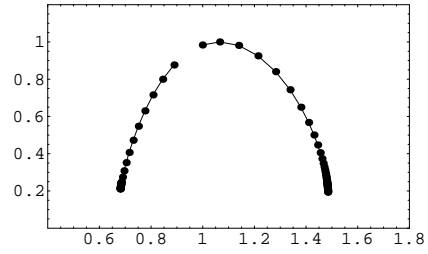
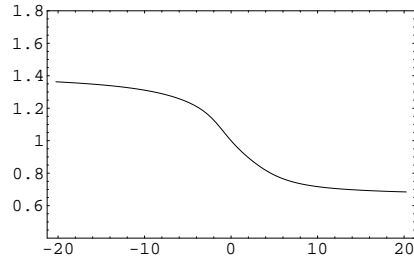
Disturbed day data, 2001



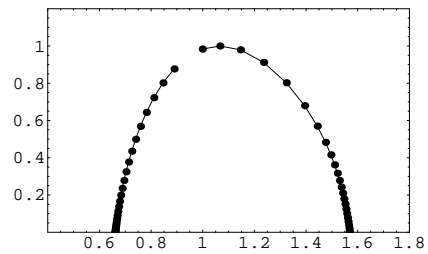
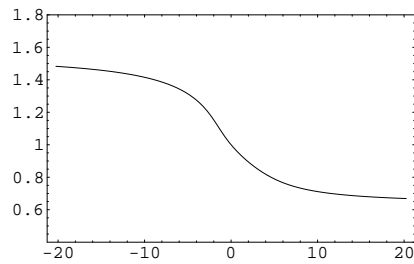
Disturbed day data, 2002



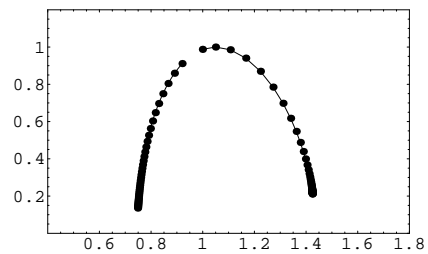
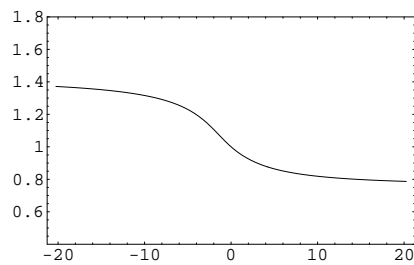
Disturbed day data, 2003



Disturbed day data, 2004



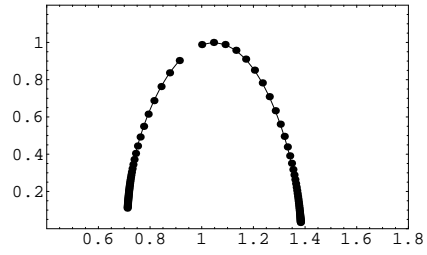
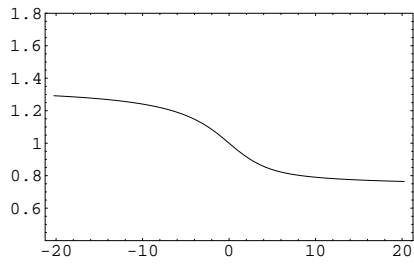
Disturbed day data, 2005



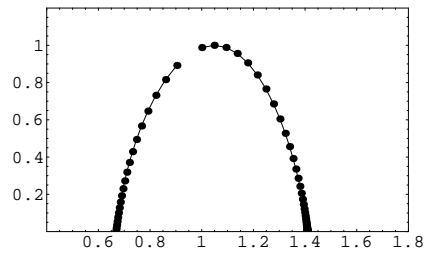
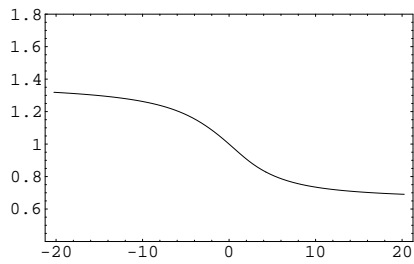
Disturbed day data, 2006

Appendix B-2: Spectra for the IMF B_y -component

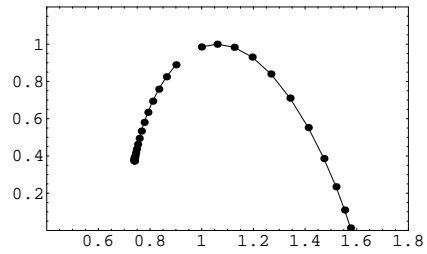
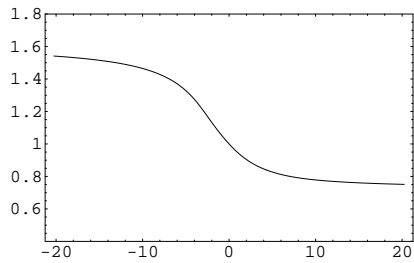
This appendix contains all the figures showing the generalized dimensions (left figures) and f - α curves (right figures) for the B_y -component of the interplanetary magnetic field for both quiet and disturbed days from 1996 to 2006.



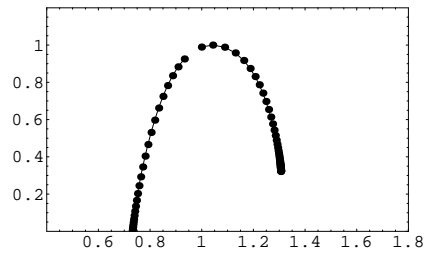
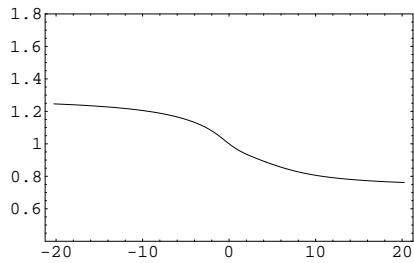
Quiet day data, 1996



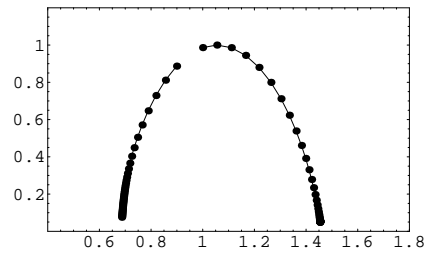
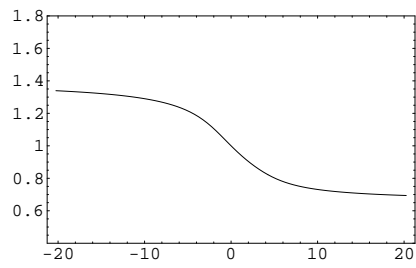
Quiet day data, 1997



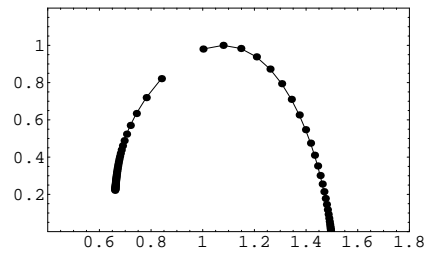
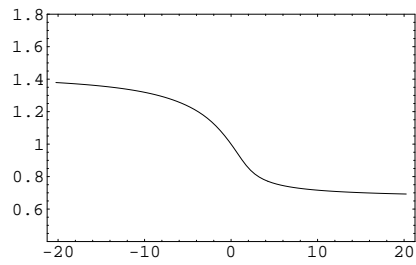
Quiet day data, 1998



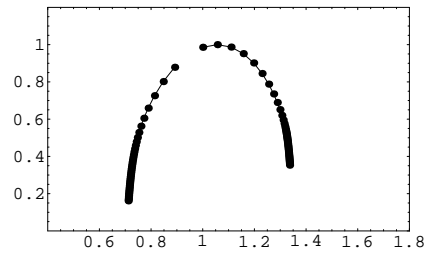
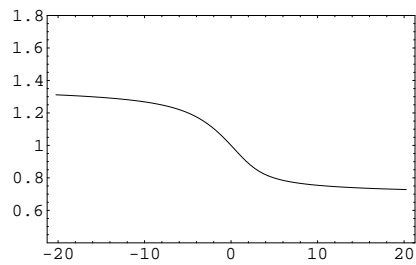
Quiet day data, 1999



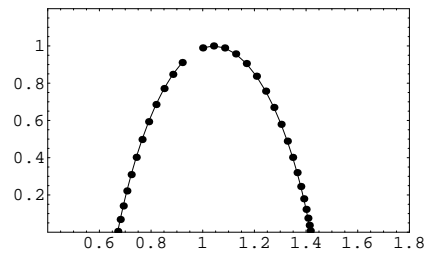
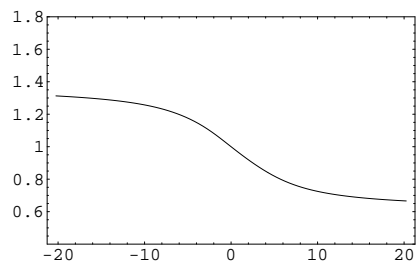
Quiet day data, 2000



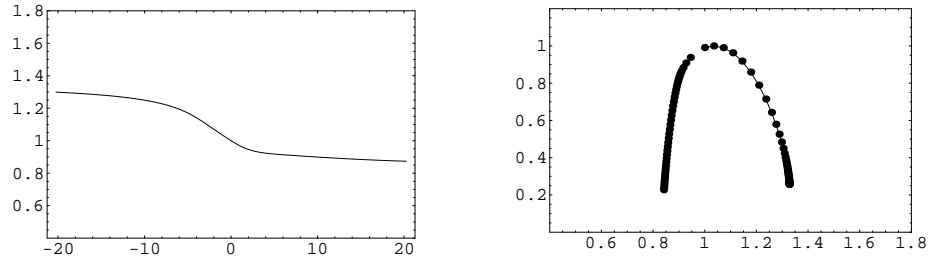
Quiet day data, 2001



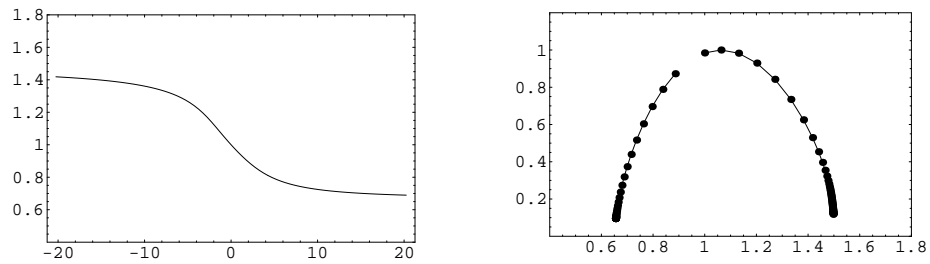
Quiet day data, 2002



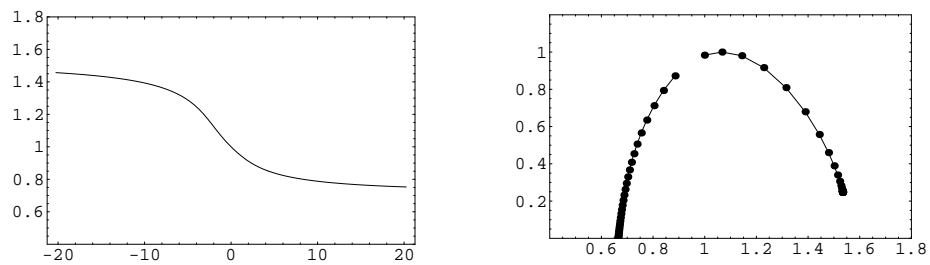
Quiet day data, 2003



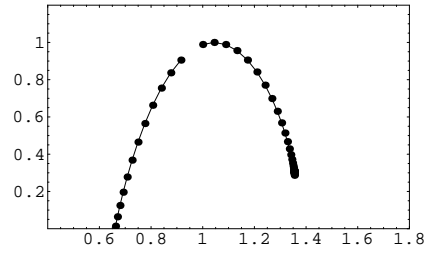
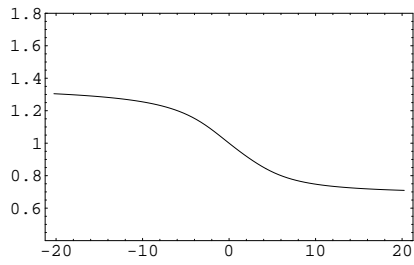
Quiet day data, 2004



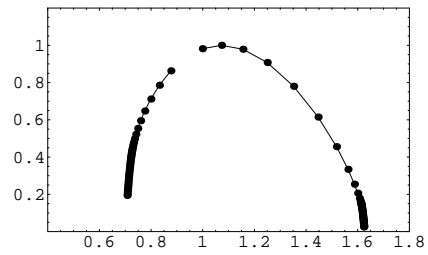
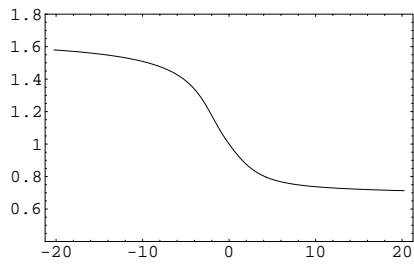
Quiet day data, 2005



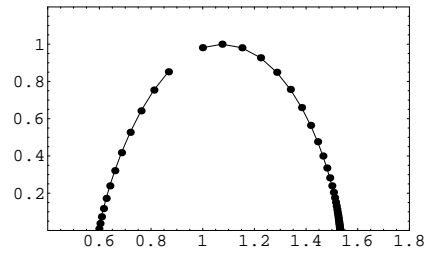
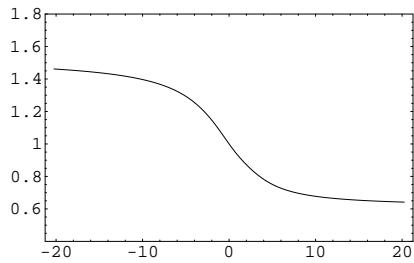
Quiet day data, 2006



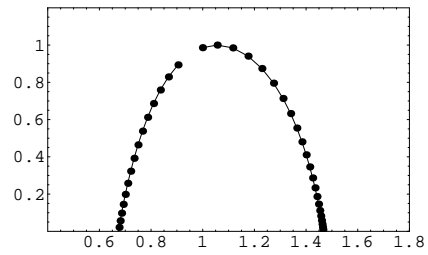
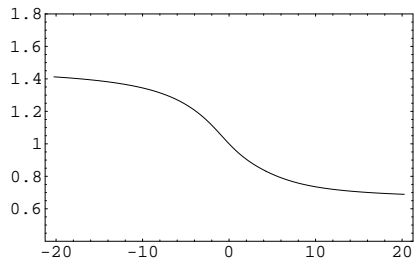
Disturbed day data, 1996



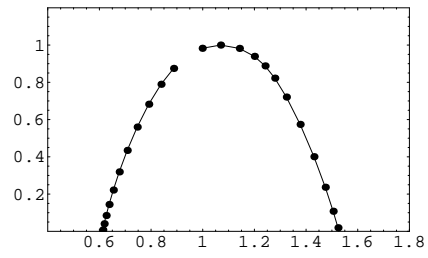
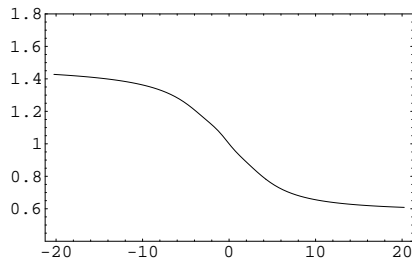
Disturbed day data, 1997



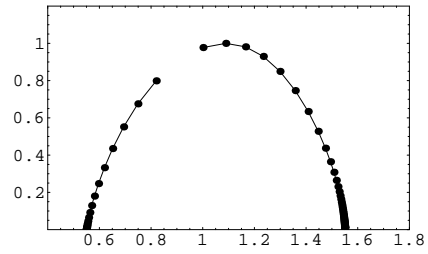
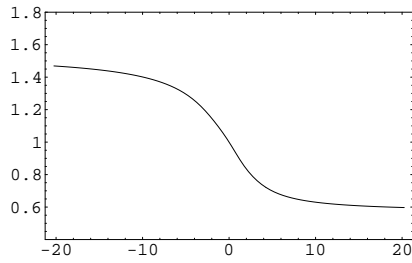
Disturbed day data, 1998



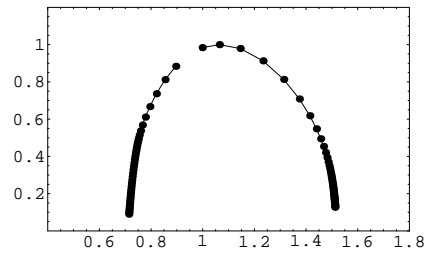
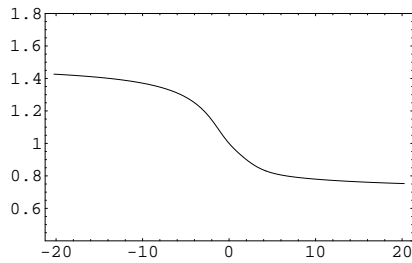
Disturbed day data, 1999



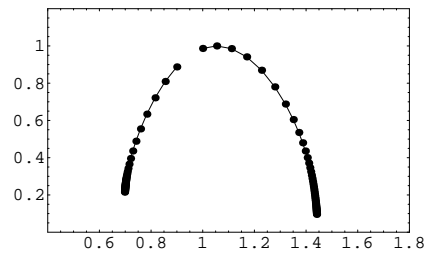
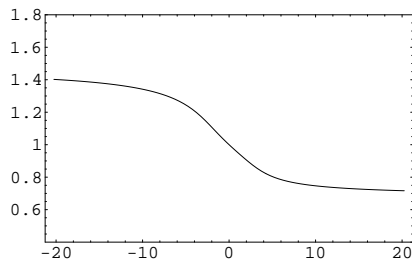
Disturbed day data, 2000



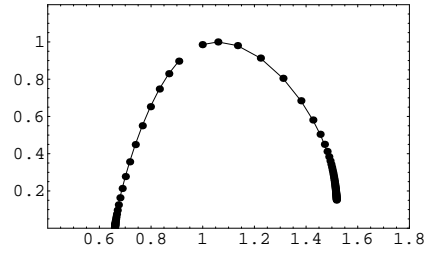
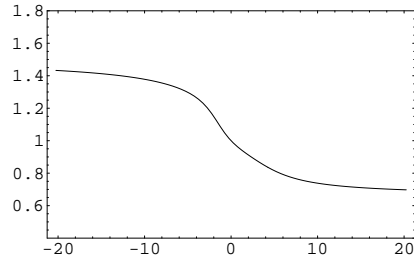
Disturbed day data, 2001



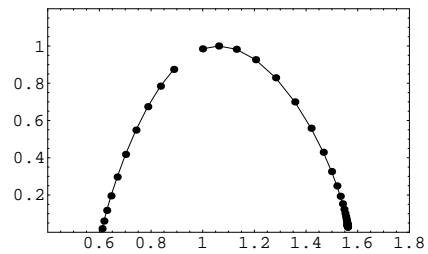
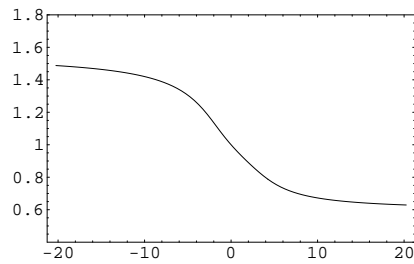
Disturbed day data, 2002



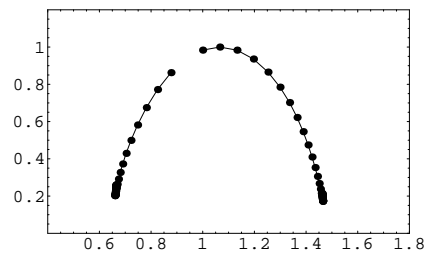
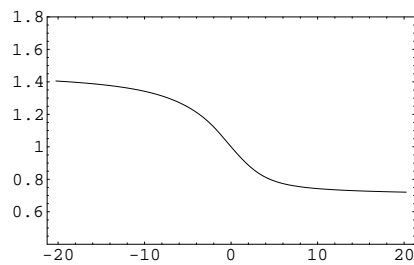
Disturbed day data, 2003



Disturbed day data, 2004



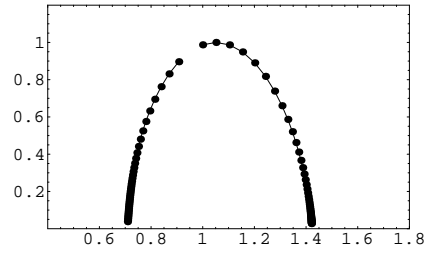
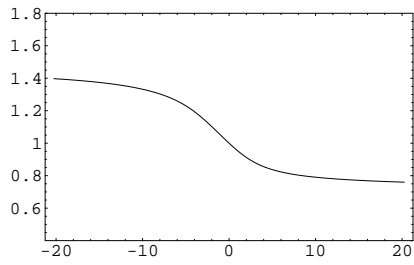
Disturbed day data, 2005



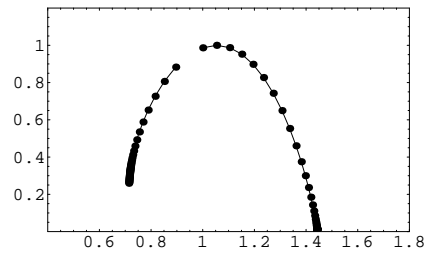
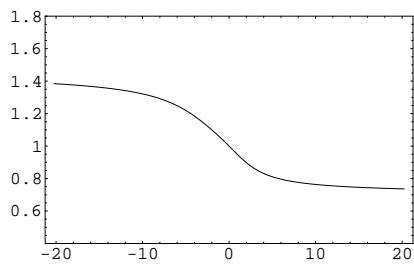
Disturbed day data, 2006

Appendix B-3: Spectra for the IMF B_z -component

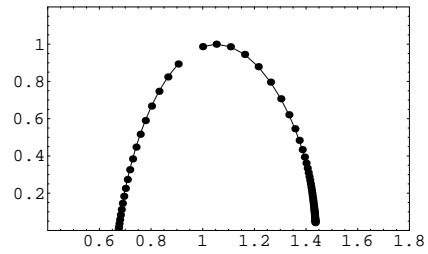
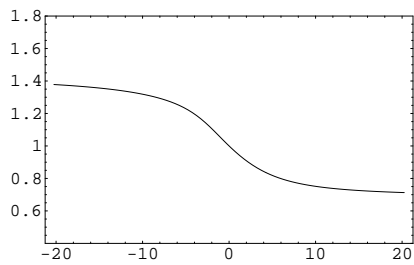
This appendix contains all the figures showing the generalized dimensions (left figures) and f - α curves (right figures) for the B_z -component of the interplanetary magnetic field for both quiet and disturbed days from 1996 to 2006.



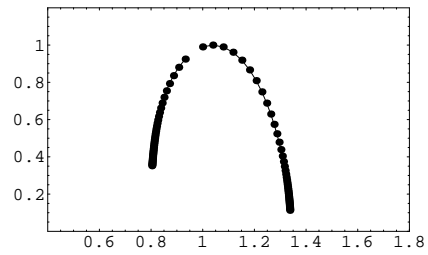
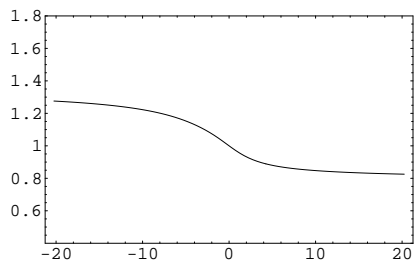
Quiet day data, 1996



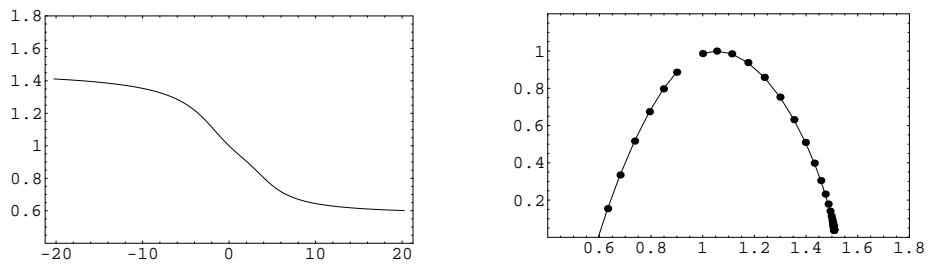
Quiet day data, 1997



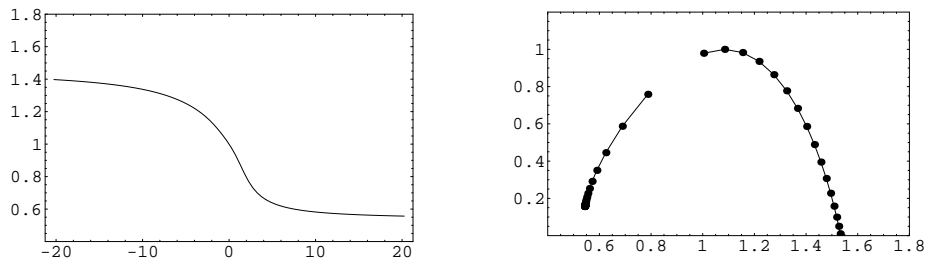
Quiet day data, 1998



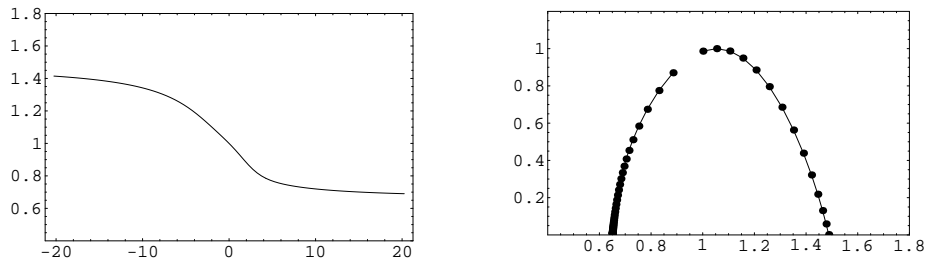
Quiet day data, 1999



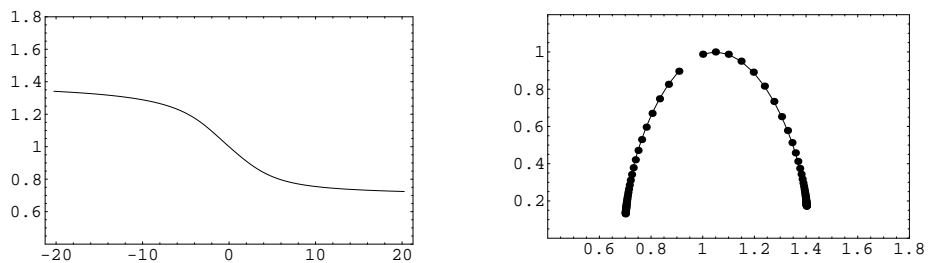
Quiet day data, 2000



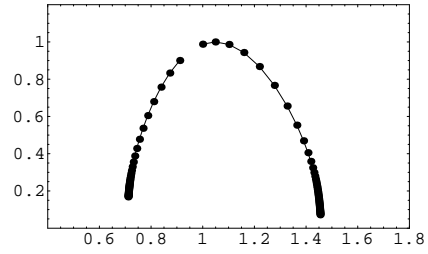
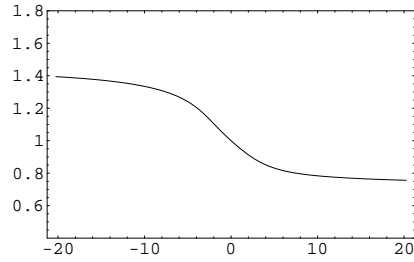
Quiet day data, 2001



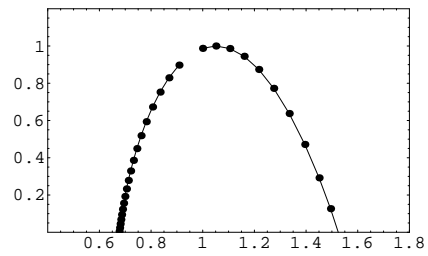
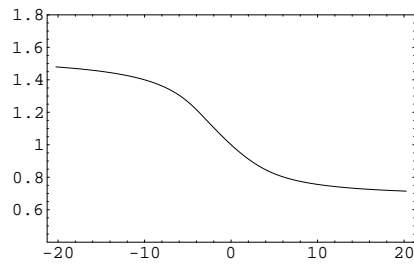
Quiet day data, 2002



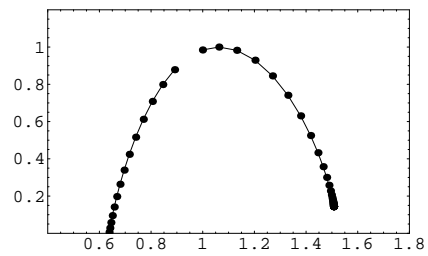
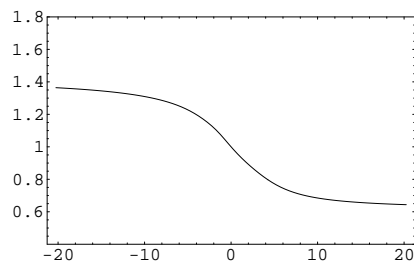
Quiet day data, 2003



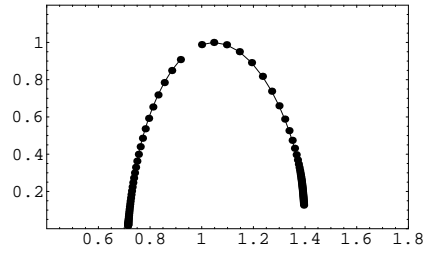
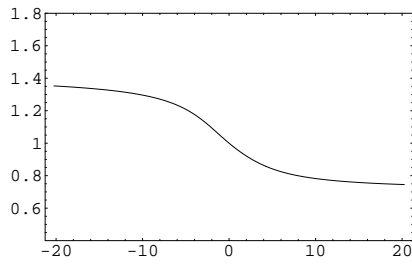
Quiet day data, 2004



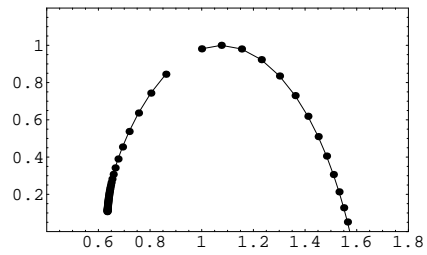
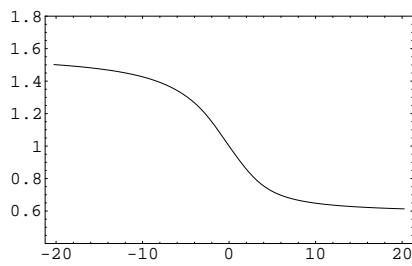
Quiet day data, 2005



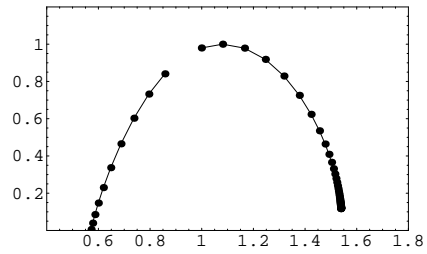
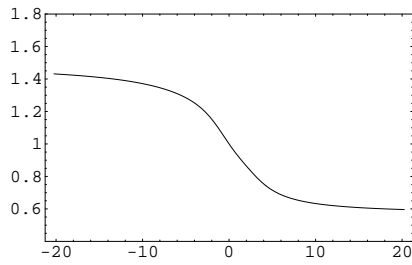
Quiet day data, 2006



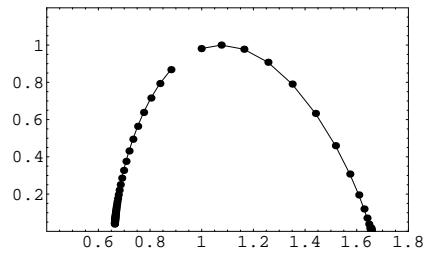
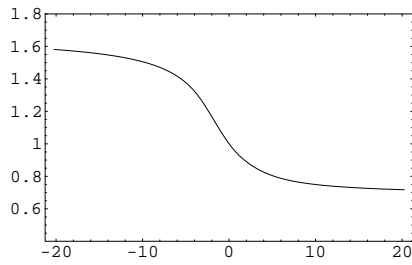
Disturbed day data, 1996



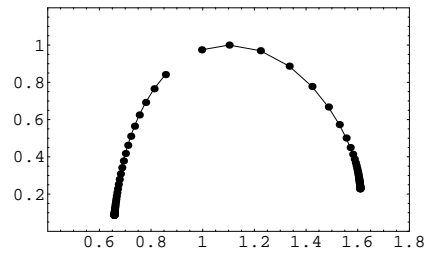
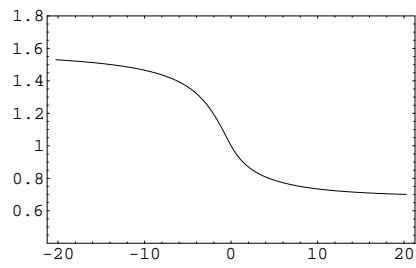
Disturbed day data, 1997



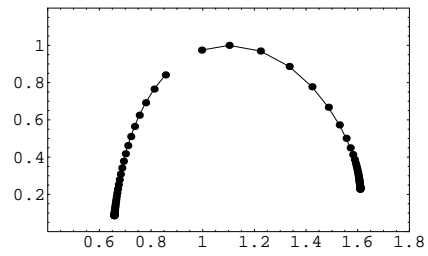
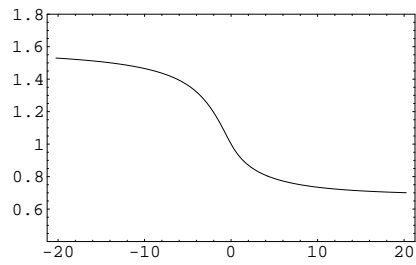
Disturbed day data, 1998



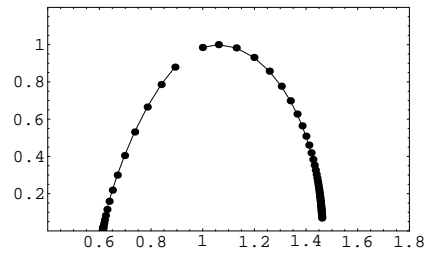
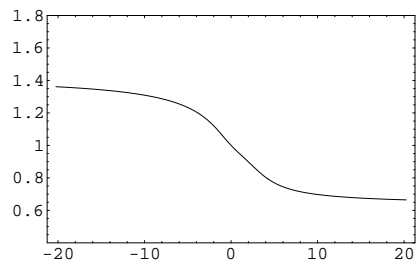
Disturbed day data, 1999



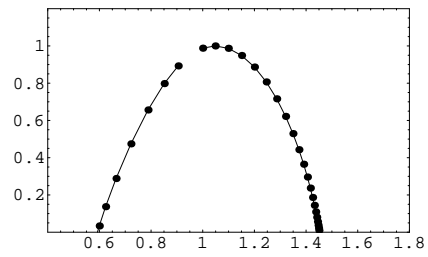
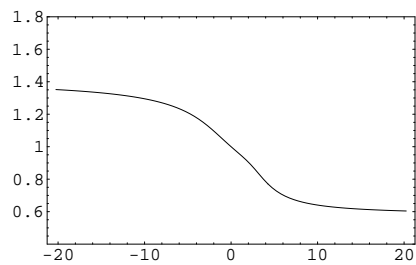
Disturbed day data, 2000



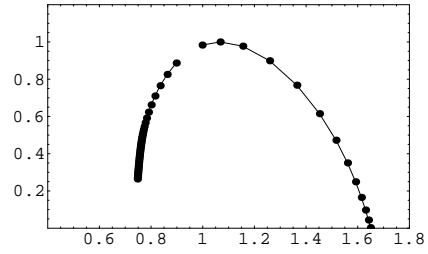
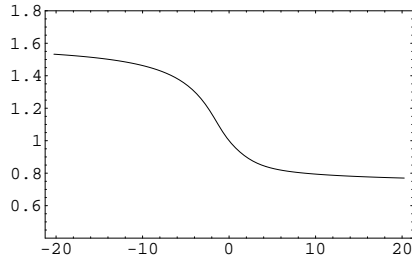
Disturbed day data, 2001



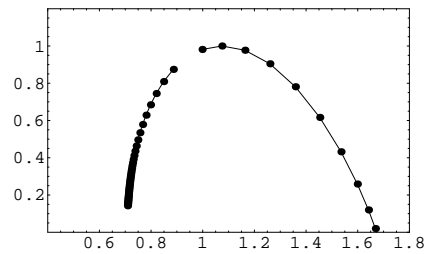
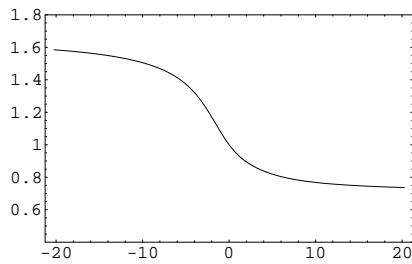
Disturbed day data, 2002



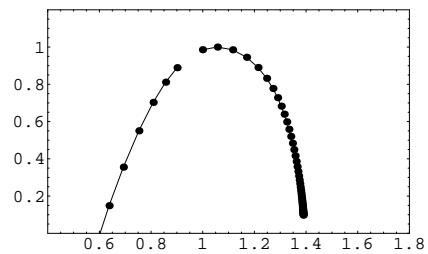
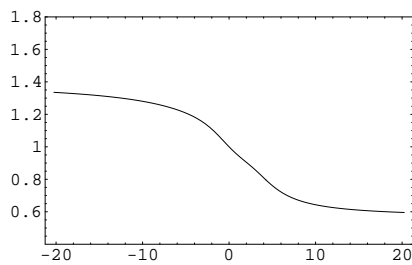
Disturbed day data, 2003



Disturbed day data, 2004



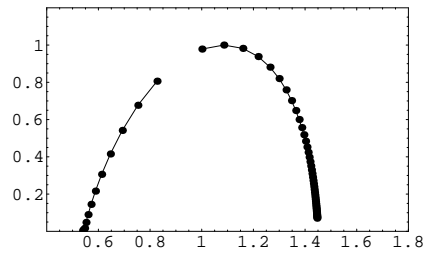
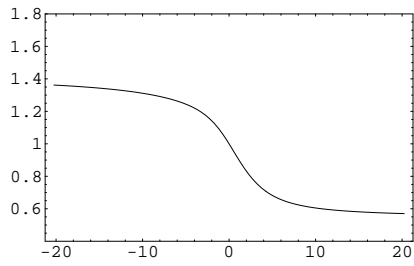
Disturbed day data, 2005



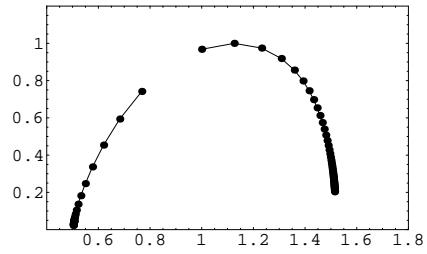
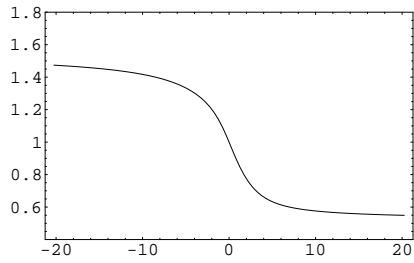
Disturbed day data, 2006

Appendix B-4: Spectra for the AE index

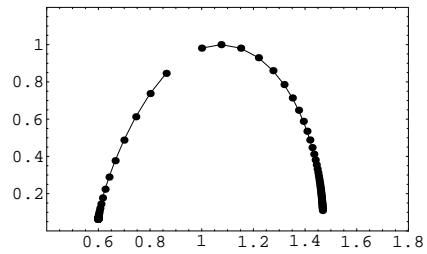
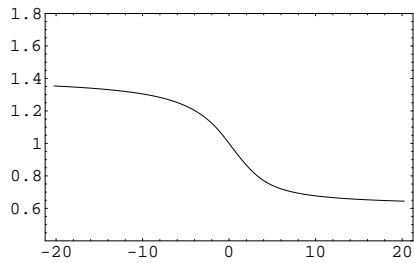
This appendix contains all the figures showing the generalized dimensions (left figures) and f - α curves (right figures) for the AE index for both quiet and disturbed days from 1997 to 2005.



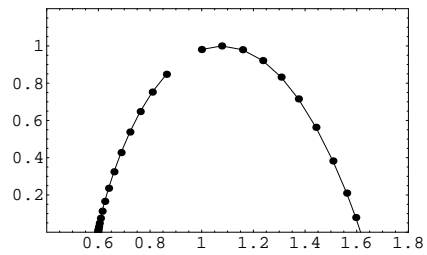
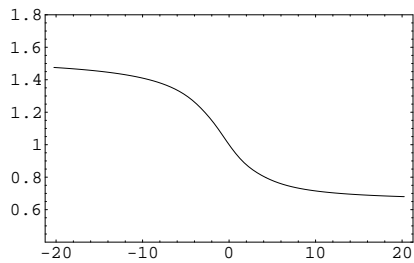
Quiet day data, 1997



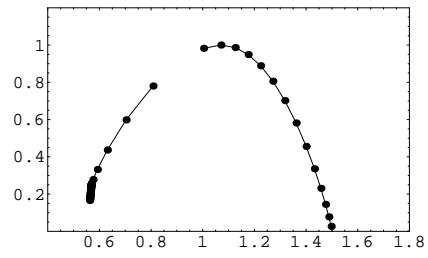
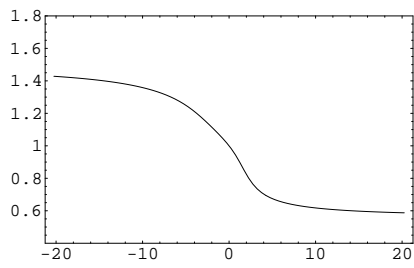
Quiet day data, 1998



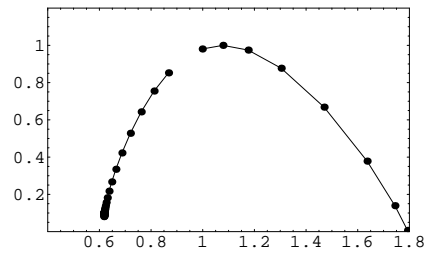
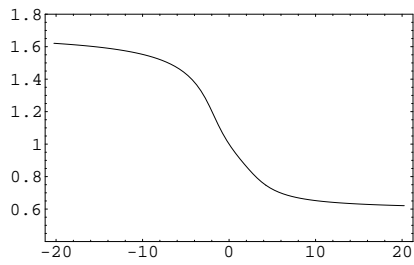
Quiet day data, 1999



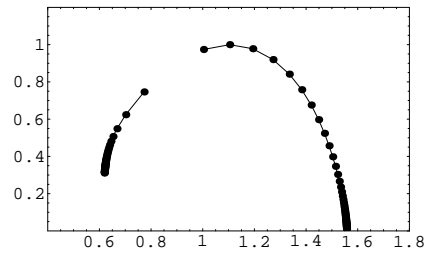
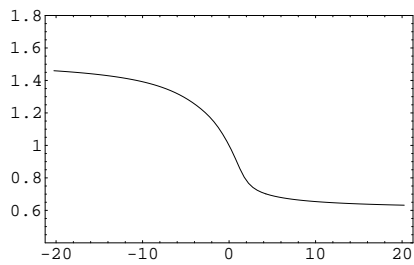
Quiet day data, 2000



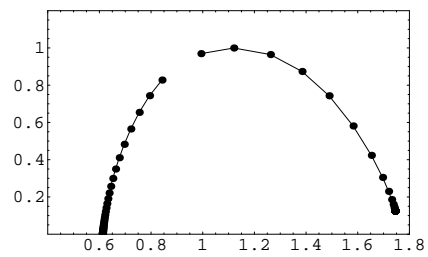
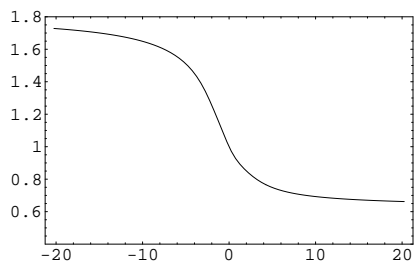
Quiet day data, 2001



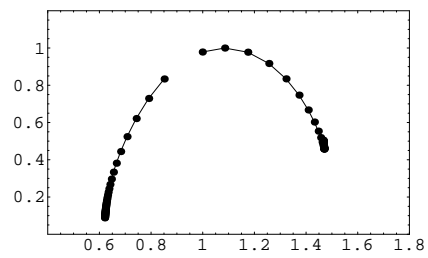
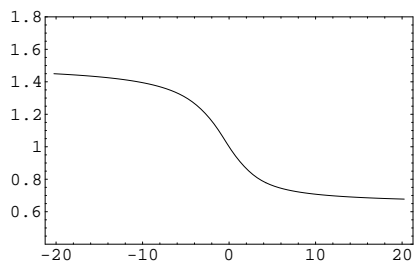
Quiet day data, 2002



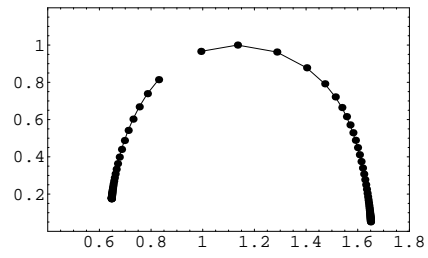
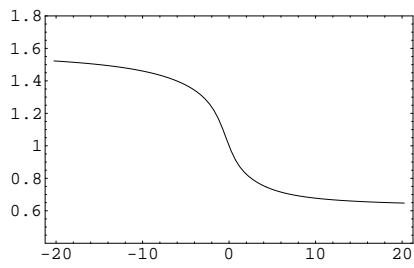
Quiet day data, 2003



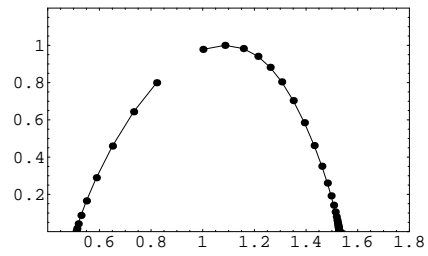
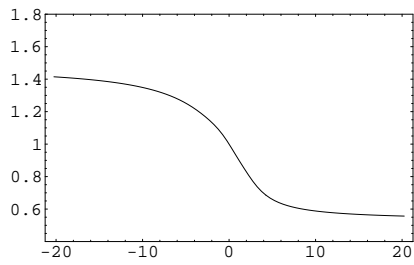
Quiet day data, 2004



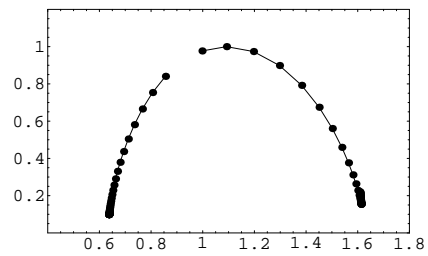
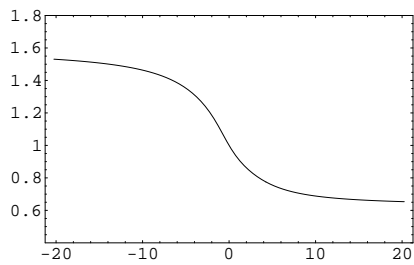
Quiet day data, 2005



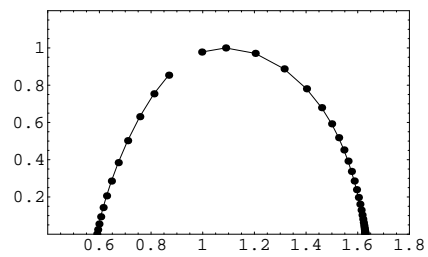
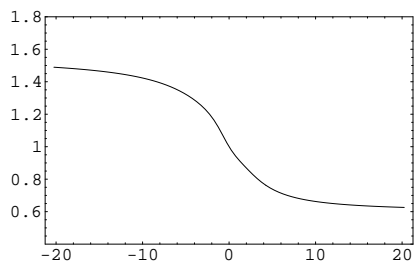
Disturbed day data, 1997



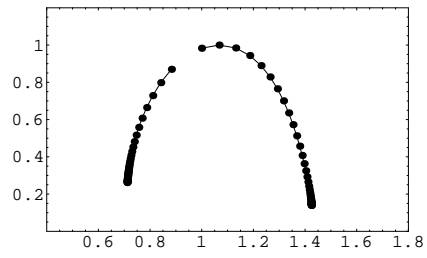
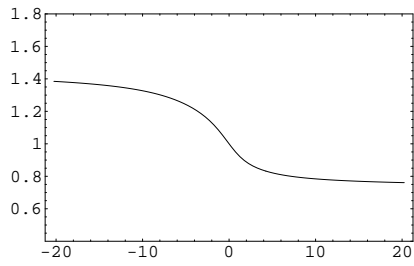
Disturbed day data, 1998



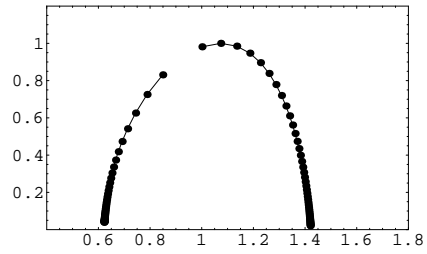
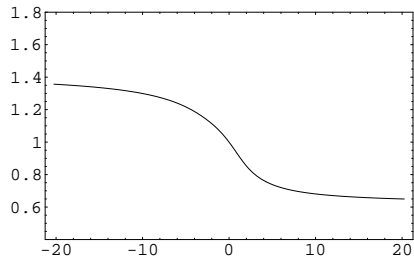
Disturbed day data, 1999



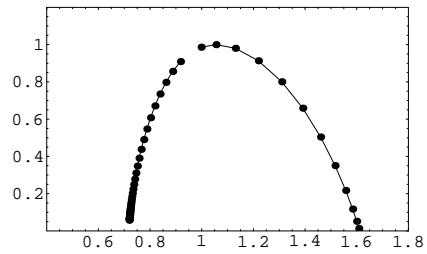
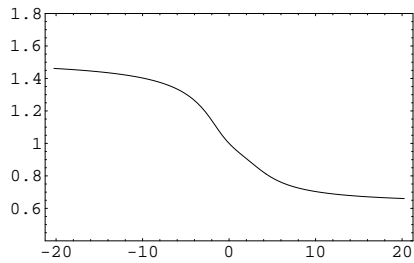
Disturbed day data, 2000



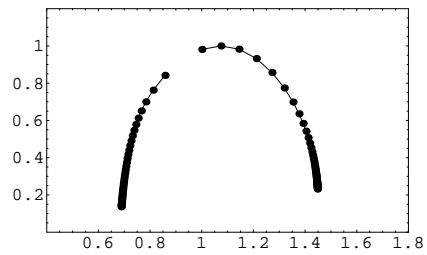
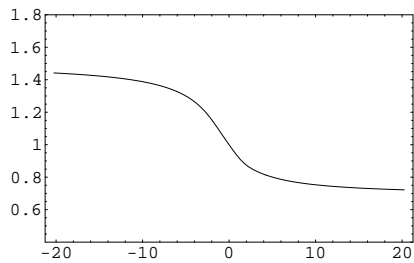
Disturbed day data, 2001



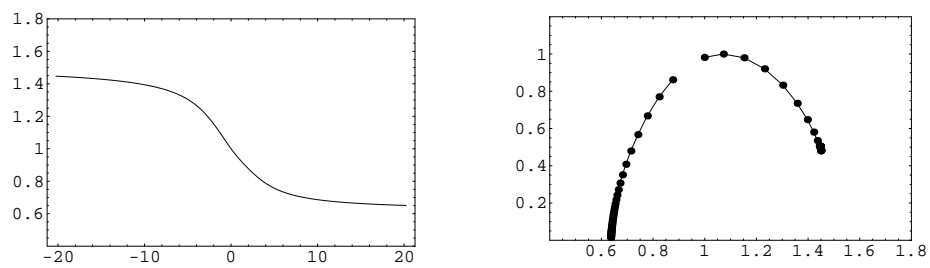
Disturbed day data, 2002



Disturbed day data, 2003



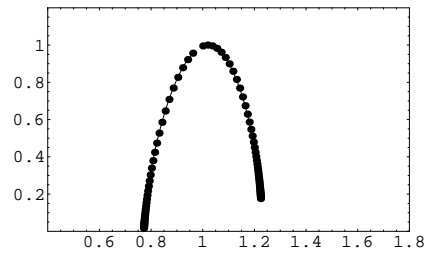
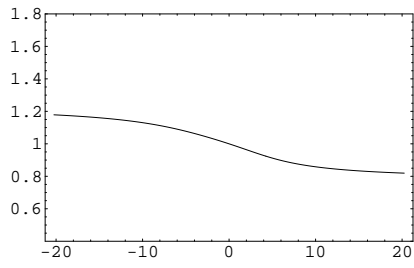
Disturbed day data, 2004



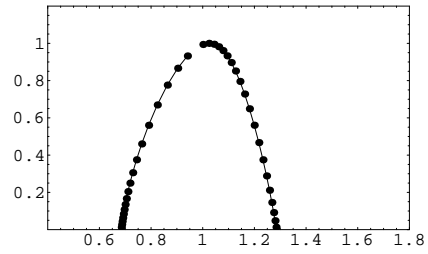
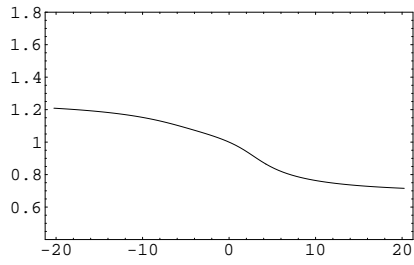
Disturbed day data, 2005

Appendix B-5: Spectra for the D_{st} index

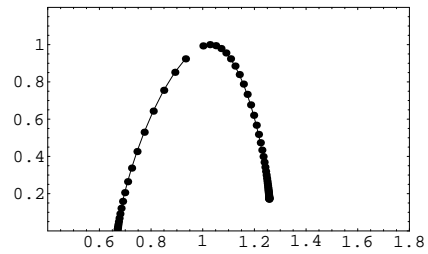
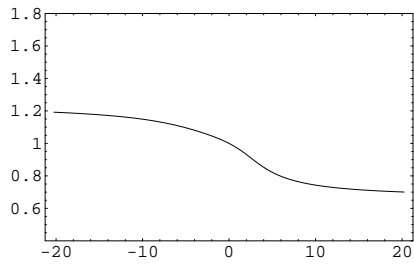
This appendix contains all the figures showing the generalized dimensions (left figures) and f - α curves (right figures) for the D_{st} index for 1996 to 2005.



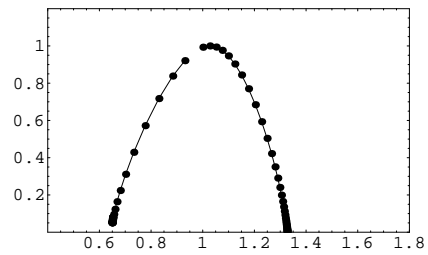
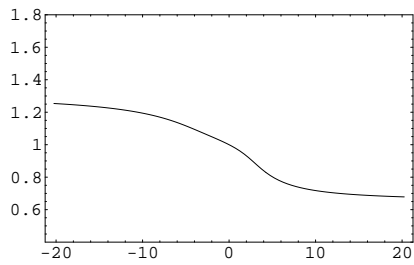
1996



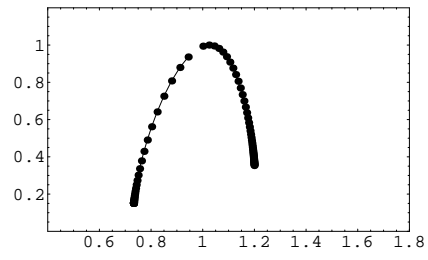
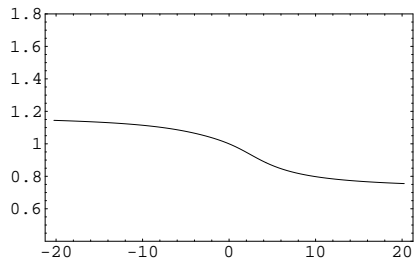
1997



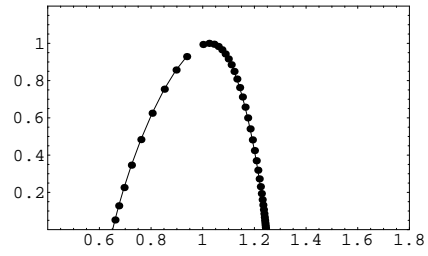
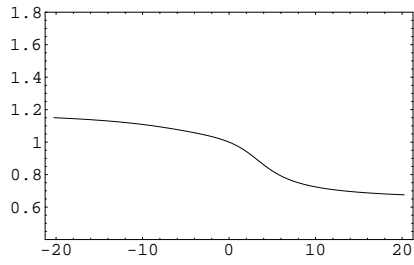
1998



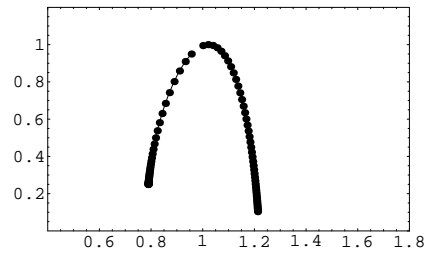
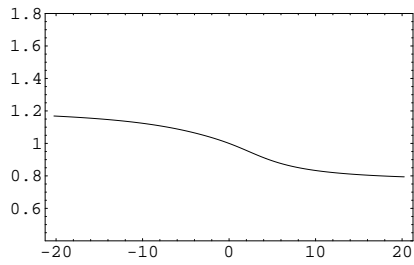
1999



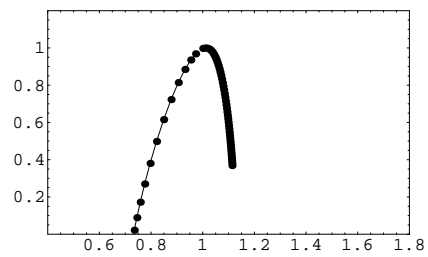
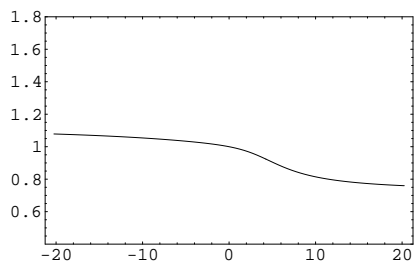
2000



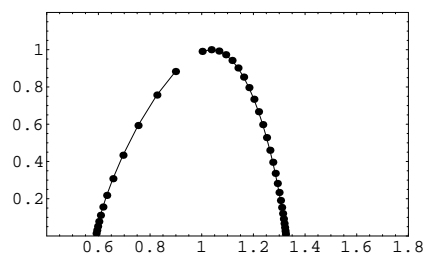
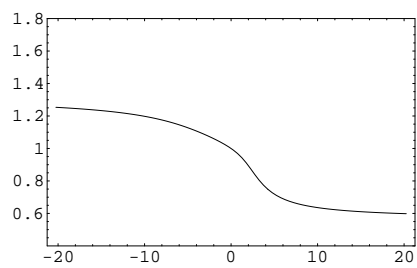
2001



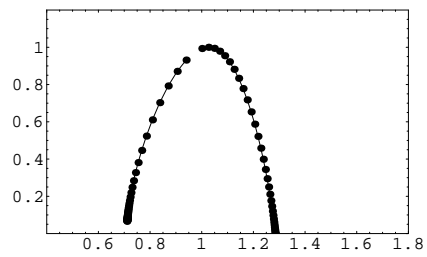
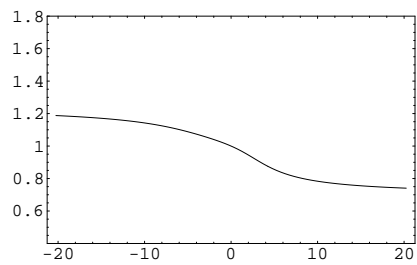
2002



2003



2004



2005

Bibliography

- [1] Turcotte, Donald L., *Fractals and Chaos in Geology and Geophysics*, Cambridge University Press, 1997, Second Edition.
- [2] Falconer, Kenneth, *Fractal Geometry - Mathematical Foundations and Applications*, Wiley, 2003, Second Edition.
- [3] Grassberger, P., Generalized Dimensions of Strange Attractors, *Physics Letters* **97A**, 227, 1983.
- [4] Halsey et al., Fractal measures and their singularities: The characterization of strange sets, *Phys. Rev. A* **33**, 1141, 1986.
- [5] Hillborn, Robert C., *Chaos and Nonlinear Dynamics, An Introduction For Scientists and Engineers*, Oxford University Press, 2000, Second Edition.
- [6] Grassberger, P. and Procaccia, I., Dimensions and Entropies of Strange Attractors From a Fluctuating Dynamics Approach, *Physica* **13D**, 34, 1984.
- [7] Sprott, Julien C., *Chaos and Time-Series Analysis*, Oxford University Press, 2003.
- [8] Turiel, A., and Pérez-Vicente, C. J., Role of multifractal sources in the analysis of stock market time series, *Physica A* **355**, 475, 2005.
- [9] Muzy, J.F. et al., Multifractal formalism for fractal signals: The structure-function approach versus the wavelet-transform modulus-maxima method, *Phys. Rev. E* **47**, 875, 1993.
- [10] Muzy, J.F. et al., Wavelets and Multifractal Formalism for Singular Signals: Application to Turbulence Data, *Phys. Rev. Lett.* **67**, 3515, 1991.
- [11] Oświęcimka, P. et al., Wavelet versus detrended fluctuation analysis of multifractal structures, *Phys. Rev E* **74**, 016103, 2006).
- [12] Geilikman, M.B. et al., Multifractal patterns of seismicity, *Earth and Planetary Sci. Lett.* **99**, 127, 1990.
- [13] Marsch, E. et al., Multifractal scaling of the kinetic energy flux in solar wind turbulence, *Ann. Geophysicae* **14**, 259, 1996.

- [14] Meneveau, C. and Sreenivasan, K. R., Simple multifractal cascade model for fully developed turbulence, *Phys. Rev. Lett.* **59**, 1424, 1987.
- [15] Burlaga, L.F., Multifractal Structure of the Interplanetary Magnetic Field, *Geophys. Res. Lett.* **18**, 69, 1991)
- [16] Yordanova, E. et al., Multifractal structure of turbulence in the magnetospheric cusp, *Ann. Geophysicae* **22**, 2431, 2004)
- [17] Solé, R.V. and Manrubia, S.C., Are Rainforests Self-organized in a Critical State?, *J. theor. Biol.* **173**, 31, 1995.
- [18] Meakin, P., Fractals, Scaling and Growth Far from Equilibrium, *Cambridge University Press*, 1998.
- [19] Udovichenko, V.V. and Strizhak, P.E., Multifractal Properties of Copper Sulfide Film Formed in Self-organizing Chemical system, *Theoretical and Experimental Chemistry* **38**, 259, 2002.
- [20] Witten, T. and Sander, L. M., Diffusion-limited aggregation, a kinetic critical phenomenon, *Phys. Rev. Lett.* **47**, 1400, 1981.
- [21] Ivanov, P.C. et al., Multifractality in human heartbeat dynamics, *Nature* **399**, 461, 1999.
- [22] Fischer, R. et al., Multi- and monofractal indices of short-term heart rate variability, *Med. Biol. Eng. Comput.* **41**, 543, 2003.
- [23] <http://cdaweb.gsfc.nasa.gov/cgi-bin/eval2.cgi>.
- [24] <http://omniweb.gsfc.nasa.gov/html/HR0docum.html>.
- [25] Fortescue, P. et al., Spacecraft Systems Engineering, *Wiley*, 2003, Third Edition.
- [26] <http://swdcwww.kugi.kyoto-u.ac.jp/aeasy/index.html>.
- [27] Bak, P., Tang, C. and Wiesenfeld, K., Self-organized criticality, *Phys. Rev. A* **38**, 364, 1988.
- [28] Campbell, W. H., Introduction to Geomagnetic Fields, *Cambridge University Press*, 2003, Second Edition.
- [29] Kivelson, M. G. and Russel, C. T., Introduction to Space Physics, *Cambridge University Press*, 1995.
- [30] Davis, T. N. and Sugiura, M., Auroral electrojet index AE and its universal time variations, *J. Geophys. Res.* **71**, 785, 1966.
- [31] http://www.gfz-potsdam.de/pb2/pb23/GeoMag/niemegk/kp_index/quietdst/.
- [32] Consolini, G. et al., Multifractal Structure of Auroral Electrojet Index Data, *Phys. Rev. Lett.* **76**, 4082, 1996.
- [33] Balasis, G. et al, From pre-storm activity to magnetic storms: a transtion described in terms of fractal dynamics, *Ann. Geophysicae* **24**, 3557, 2006.

- [34] Živković, T., Østvand, L. and Rypdal, K., On the Connection Between the Multifractality and the predictability From the Auroral Index Time Series, *Publ. Astron. Obs. Belgrade* No. 87 (2008), 1 - 4, Contributed paper, 2008.